Migrating diurnal tide anomalies during QBO disruptions in 2016 and 2020: morphology and mechanism

Shuai Liu[1,2], Guoying Jiang[1,3,4], Bingxian Luo[1,2], Xiao Liu[5], Jiyao Xu[1,3], Yajun Zhu[1,3,4], Wen Yi[6,7]

[1]State Key Laboratory of Solar Activity and Space Weather, National Space Science Center, Chinese Academy of Sciences, Beijing, 100190, China
[2]College of Earth and Planetary Sciences, University of Chinese Academy of Sciences, Beijing, 101408, China
[3]School of Astronomy and Space Science, University of Chinese Academy of Sciences, Beijing, 101408, China
[4]Hainan National Field Science Observation and Research Observatory for Space Weather, Danzhou, Hainan Province, China.
[5]School of Mathematics and Statistics, Henan Normal University, Xinxiang, 453007, China
[6]CAS Key Laboratory of Geospace Environment, Department of Geophysics and Planetary Sciences, University of Science and Technology of China, Hefei, China
[7]CAS Center for Excellence in Comparative Planetology, Anhui Mengcheng Geophysics National Observation and Research Station, University of Science and Technology of China, Hefei, China

Correspondence to: Guoying Jiang (gyjiang@swl.ac.cn) and Bingxian Luo (luobx@nssc.ac.cn)

Abstract. The stratosphere Quasi-Biennial Oscillation (QBO) modulates the migrating diurnal tide (DW1) in the mesosphere and lower thermosphere (MLT). DW1 amplitudes are larger during QBO westerly (QBOW) than during easterly (QBOE) phases. Since QBO's discovery in 1953, two rare QBO disruption events occurred in 2016 and 2020. During these events, anomalous westerly winds propagate upward, disrupting normal downward propagation of easterly phase and producing a persistent westerly wind layer. In this study, global responses of DW1 amplitudes and phases in MLT to these QBO disruptions, as well as its underlying mechanisms are investigated, using SABER/TIMED observations, MERRA-2 reanalysis and SD-WACCM-X simulations. Similarity of the DW1 responses to these two events is that DW1 phases and wavelengths exhibit close results to QBOW, whereas the amplitudes show significant responses. Relative to regular QBOE, DW1 amplitudes increase by ~20.5 % at equator and ~14.4 % at 30°N/S during the 2016 event, but by only ~6.0 % and ~7.7 % during the 2020 event. In 2016 event, water vapor radiative and latent heating increased by ~8 % and ~22 % relative to QBOE. The zonal wind latitudinal shear and gravity-wave (GW) drag tend to enhance DW1 amplitudes. In contrast, in 2020 event, only water vapor radiative heating exhibits a ~5 % increase. The zonal wind latitudinal shear has less effect on DW1, while GW drag exerts a comparatively weaker influence. The modest enhancement of water vapor heating together with the weaker GW drag likely accounts for the weaker enhancement of DW1 during this event.

1 Introduction

Atmospheric solar tides are planetary-scale harmonic waves with periods of a solar day. In the mesosphere and lower thermosphere (MLT), solar tides exert significant influences on atmospheric parameters such as wind, temperature, and density

(Chapman & Lindzen, 1980; Xu et al., 2009; Jiang et al., 2010; Smith, 2012). Among these tides, the migrating diurnal tide (DW1) is one of the most prominent components. DW1 in MLT is modulated by external forcings, including the stratosphere Quasi-Biennial Oscillation (QBO, Hagan et al., 1999; Wu et al., 2008; Xu et al., 2009; Oberheide et al., 2009; Mukhtarov et al., 2009; Davis et al., 2013; Gan et al. 2014), El Niño–Southern Oscillation (ENSO, Lieberman et al., 2007; Cen et al., 2022) and 11-year solar cycle response (Singh and Gurubaran, 2017; Sun et al., 2022; Liu et al., 2024a; Liu et al., 2024b). In this work, the impact of QBO is focused.

The QBO dominates the variability of the equatorial stratosphere (∼16–50 km), shown as alternating downward propagating easterly wind (so-called QBO easterly phases) and westerly wind (so-called QBO westerly phases), with an averaging period of approximately 28 months (Baldwin et al., 2001). QBO is driven by vertically propagating Kelvin, mixed Rossby gravity waves and small-scale gravity waves (Lindzen and Holton, 1968; Holton and Lindzen, 1972; Baldwin et al., 2001; Ern et al., 2014). It could influence the transport and distribution of trace gases like water vapor and ozone in the troposphere and stratosphere (Schoeberl et al., 2008).

During the winter of 2015/16 and 2019/20, two rare stratospheric QBO disruption events occurred, which were found only twice since the record began in 1953. The events are manifested by anomalous westerly winds propagating upward, disrupting normal downward propagation of the easterly phase and producing a persistent westerly wind layer (Newman et al., 2016; Anstey et al., 2021). The 2016 QBO disruption has been confirmed to have a close causal relationship with the 2015/16 extreme El Niño event (Newman et al., 2016; Osprey et al., 2016; Barton and Mccormack, 2017; Coy et al., 2017). The 2015/16 El Niño substantially weakened the subtropical easterly jet, allowing enhanced Rossby wave propagation from the extratropics into the deep tropics near 40 hPa (Barton and Mccormack, 2017). These amplified Rossby waves subsequently broke and deposited momentum near the QBO westerly core, rather than at the climatological zero-wind line, causing a pronounced deceleration. The deceleration gave rise to a persistence of westerlies at 40–15 hPa, preventing the expected transition to easterlies and ultimately leading to the QBO disruption (Newman et al., 2016; Osprey et al., 2016; Coy et al., 2017; Barton and Mccormack, 2017; Kang et al., 2022; Wang et al., 2023). The QBO disruption was accompanied by a marked strengthening of the Brewer–Dobson residual circulation, thereby intensifying tropical upwelling. This upwelling contributed to an upward displacement of westerlies in the tropical lower stratosphere (Coy et al., 2017), modifying the transport and distribution of trace gases such as water vapor. The persistent westerlies also created conducive background conditions for the vertical propagation of DW1. Nevertheless, not all strong El Niño events trigger QBO disruptions. In the 2015/16 case, the QBO westerly wind core was weaker and Rossby wave activity stronger than in other extreme events, such as the 1998 El Niño (Barton and Mccormack, 2017). In 2020 event, the upward-propagating westerly wind is so weak that the monthly mean zonal wind is shown as upward-propagating easterly wind (e.g. Anstey et al., 2021; Wang et al., 2023). This event is driven by strong extratropical Rossby waves associated with the 2019 minor SSW in south hemisphere (Kang and Chun, 2021; Wang et al., 2023). In these two events, the trace gases like ozone and water vapor are modulated. During the 2016 QBO disruption event, positive water vapor anomalies were observed between the tropopause and lower stratosphere, while positive ozone anomalies appeared in the upper stratosphere (Tweedy et al., 2017; Diallo et al., 2018). A similar pattern was reported for the 2020 disruption event, with water vapor in the lower stratosphere and ozone in the upper stratosphere also exhibiting positive anomalies (Diallo et al., 2022).

QBO modulation of diurnal tides has been reported by both ground-based and space-borne observations (Araújo et al., 2017; Davis et al., 2013; Pramitha et al., 2021b; Wu et al., 2008; Dhadly et al., 2018). Mayr and Mengel (2005) reported that the QBO can affect these amplitudes by up to 30 % using the Numerical Spectral Model (NSM). Thermosphere, Ionosphere, Mesosphere Energetics and Dynamics/Sounding of the Atmosphere using Broadband Emission Radiometry (TIMED/SABER) observations revealed that the quasi-biennial variability of DW1 could exceed 50 % at certain altitudes (Garcia, 2023). The modulation was characterized by larger-than-average diurnal tide amplitudes during the westerly phase of the QBO and smaller-than-average amplitudes during the easterly phase (Vincent et al., 1998; Wu et al., 2008; Xu et al., 2009; Davis et al., 2013; Araújo et al., 2017; Pramitha et al., 2021b; Garcia, 2023). Several mechanisms have been proposed could be considered for modulating the migrating diurnal tide (DW1). A primary factor emphasized in many studies is the variation in the background zonal wind and its latitudinal shear (Forbes and Vincent, 1989; Hagan et al., 1999; McLandress, 2002b; Riggin and Lieberman, 2013; Liu et al., 2015; Ortland, 2017; Dhadly et al., 2018; Pramitha et al., 2021a, b). Forbes and Vincent (1989) demonstrated that the DW1 (1,1) mode experiences stronger dissipation in easterly phases than in westerly phases, while McLandress (2002b) highlighted the tide's strong sensitivity to latitudinal shears in the zonal mean easterlies of the summer mesosphere. Apart from the influence of the background wind, additional contributions have been suggested, including variations in diurnal heating (McLandress, 2002b; Riggin and Lieberman, 2013; Ortland, 2017) and tide–gravity wave (GW) interactions (Mayr et al., 1998; McLandress, 2002a; Lu et al., 2012; Wang et al., 2024), both of which may play a role in modulating the QBO-related variability of DW1.

Recent studies have shown that the diurnal tides were also modulated during the QBO disruption events (Pramitha et al., 2021a; Garcia, 2023; Wang et al., 2024). Pramitha et al. (2021a) first reported the enhancement of the diurnal tides during the 2015/2016 QBO disruption event using meteor radar over Tirupati (13.63°N, 79.4°E) and linked this enhancement to changes in ozone concentration. Garcia (2023) showed the equatorial response of temperature DW1 to these two disruption events when analysing the QBO modulation to DW1. Wang et al. (2024) reported the weakened mesospheric diurnal tides at mid-latitude during QBO disruption events, which is observed by a meteor radar chain. They further gave the modulation evidence of gravity wave forcing and solar radiative absorption by subtropical stratospheric ozone revealed by SD-WACCM-X simulations.

These findings raise three questions: (1) In addition to the equatorial peak, temperature DW1 exhibits secondary amplitude maxima at 30°N and 30°S (Xu et al., 2009; Garcia, 2023). Whether the DW1 amplitudes on a global scale show a similar response to the QBO disruption events. (2) Whether the phases and wavelengths of DW1 could be affected by the events. (3) (3) Mechanisms for modulating DW1 include heating sources such as water vapor radiative heating and latent heating, zonal wind latitudinal shear, and tide–gravity wave interactions (e.g., Forbes and Vincent, 1989; Hagan, 1996; Hagan et al., 1999; McLandress, 2002a; Kogure and Liu, 2021). Whether these mechanisms play significant roles in modulating DW1 during QBO disruption events.

The present study will focus on the global response feature of DW1 and its underlying mechanisms to QBO disruption events. The response of DW1 amplitudes, phases and wavelengths during the event will be investigated. Moreover, the contribution of possible mechanisms, including heating sources, the zonal wind latitudinal shear and tidal-gravity wave during the event, will be explored. The article is organized as follows: Section 2 introduces TIMED/SABER, SD-WACCM-X, MERRA-2 data and the methodologies to extract the migrating tides. Section 3 presents the response feature of the DW1 to the QBO disruption events revealed by SABER/TIMED observations and SD-WACCM-X simulation results. The possible mechanism of DW1 response to the disruption events is discussed in Section 4. Section 5 presents the summary.

2 Data and methodology

This study employs the dataset of SABER/TIMED observations, SD-WACCM-X simulations and MERRA-2 reanalysis to reveal the feature of DW1 and its excitation sources during QBO disruption events. DW1 amplitude, phase, and wavelength are derived from both SABER/TIMED data and SD-WACCM-X outputs. MERRA-2 reanalysis is used to analyse the contributions of water vapor radiative heating and latent heating to DW1 variability during the QBO disruption events, while SABER/TIMED observations characterize ozone radiative heating. SD-WACCM-X simulations validate the excitation source revealed by the observational datasets.

2.1 SABER/TIMED observations

The TIMED satellite is in a near sun-synchronous orbit with a 73° inclination at about 625 km. The number of orbits observed per day is about 15. SABER, an instrument in the TIMED satellite, is a 10-channel broadband (1.27–17 μm) limb-scanning infrared radiometer. SABER observations of infrared radiance are used to retrieve kinetic temperature, trace gases, etc. In this work, kinetic temperature and ozone observations in level 2 A (L2A) dataset and ozone heating rate in level 2B (L2B) dataset are selected to analyse the DW1 response to QBO disruption events. Kinetic temperature is derived using a full nonlocal thermodynamic equilibrium (non-LTE) inversion algorithm (Mertens et al., 2001; 2004) with the combination of the measured 15 μm CO_2 vertical emission profile and CO_2 concentrations provided by the Whole Atmosphere Community Climate Model (WACCM 3.5.48) described in Garcia et al. (2007).

It takes SABER 60 days to sample 24 hours in local time. The data latitudinal coverage every 60 days extends from 53°N to 83°S or 53°S–83°N. Temperature observations taken from version 2.07 data from 2002 to 2019 and version 2.08 data from 2020 to 2023 are used. The details of the version switches could refer to Mlynczak et al. (2022, 2003). The retrieved temperature observations used in this work cover altitudes from approximately 15 km to 105 km.

2.2 SD-WACCM-X

The Whole Atmosphere Community Climate Model with thermosphere–ionosphere eXtension (WACCM-X) is a comprehensive numerical model that could simulate the Earth's atmosphere from the surface up to the upper thermosphere

(~500–700 km), including the ionosphere (Liu et al., 2010; 2018). WACCM-X is a single, unified whole-atmosphere model that extends the NCAR Whole Atmosphere Community Climate Model (WACCM4; Marsh et al., 2013). WACCM4 itself built upon the Community Atmosphere Model 4 (CAM4; Neale et al., 2013). While the thermosphere–ionosphere physics (e.g., global electrodynamo, O^+ transport, electron/ion energetics) incorporated in WACCM-X were largely adapted from the NCAR Thermosphere–Ionosphere–Electrodynamics General Circulation Model (TIE-GCM; Qian et al., 2014; Pedatella, 2022), they have been re-engineered within the WACCM-X dynamical core and coupled to the lower- and middle-atmosphere processes through a dedicated ionosphere-interface module. SD in the SD-WACCM-X means specified dynamics, which is an approach described in Smith et al. (2017). The reanalysis fields from Modern-Era Retrospective analysis for Research and Applications, Version 2 (MERRA-2, Gelaro et al., 2017) data from the surface up to ~50 km are nudged in WACCM-X. Model parameters are output in 3-hour resolution. The latitude-longitude resolution is 1.9°×2.5°. The model has 145 pressure levels with a varying vertical resolution of ∼1.1–1.75 km in the troposphere and stratosphere and ∼3.5 km in the mesosphere. In this work, the temperature, zonal wind, temperature tendency due to moist process and long wave heating rate ranging from 2002 to 2022 are selected.

2.3 MERRA-2

MERRA-2 is a reanalysis product from the NASA Global Modeling and Assimilation Office (GMAO) and provides data like wind, temperature, mixing ratio of components, and so on. (Gelaro et al., 2017). In this work, the zonal wind, temperature, air density, surface albedo, water vapor mixing ratio and temperature tendency due to moist process range from 2002 to 2023 are selected. The time resolution is 3-hour per day. The spatial resolution is a 2.5°×2.5° latitude-by-longitude grid at 72 model levels from ground to 0.01 hPa.

2.4 Singapore radiosonde QBO index

The QBO index employed in this study is derived from Singapore radiosonde measurements obtained by the Meteorological Service Singapore Upper Air Observatory (station 48698; 1.34°N, 103.89°E; 21 m above mean sea level). The monthly mean zonal wind data processed by the National Aeronautics and Space Administration/Goddard Space Flight Center (NASA/GSFC) is selected, spanning 2002–2023 at pressure levels between 100 hPa and 10 hPa.

2.5 Water vapor radiative heating rate calculation

Troposphere heating by water vapor absorption of near-infrared radiation is an important excitation source for DW1 (Hagan, 1996; Lieberman et al., 2003). Due to the SABER's observational gap in the troposphere, the MERRA-2 dataset is adopted. In this dataset, temperature, air density, surface albedo, cloud fraction and water vapor mixing ratio (specific humidity) are the variables necessary for the calculation. The heating rate is the sum of clear sky and cloudy sky (Groves et al., 1982):

$$J = (1 - k)J_{clear} + kJ_{cloudy} \quad (1)$$

where k is the cloud fraction, J_{clear} and J_{cloudy} are the heating rates of the clear sky and cloudy sky. The calculation equations for clear sky and cloudy sky are given in Appendix A.

2.6 Ozone radiative heating rate calculation

The calculation of ozone radiative heating follows the Strobel/Zhu scheme (Strobel, 1978; Zhu, 1994), in which the total heating rate is obtained as the sum of contributions from the Hartley, Huggins, and Chappuis bands, with parameterizations from Zhu (1994). The required ozone volume mixing ratio (VMR) and density are taken from the SABER L2A dataset. Ozone VMR is retrieved from vertical emission profiles at 9.6 µm and 1.27 µm (Smith et al., 2013). The former covers all local times and the latter is limited to daytime. In this study, the 9.6 µm retrievals are used. It should be noted that the Strobel/Zhu model omits the dominant nighttime chemical-heating source between ~70 and 100 km (Zhu, 1994; Xu et al., 2010). Consequently, the present analysis is restricted to the sum of the three-band heating rates between 20 and 70 km.

2.7 Method for extracting DW1 and data processing

Non-uniform SABER observational data were processed into zonal mean data and used to extract tides. The procedures are introduced briefly as follows. Firstly, the kinetic temperature, ozone mixing ratio and ozone radiative heating rate profiles are interpolated vertically with a 1 km spacing. Profiles of each day are sorted into ascending and descending groups. Secondly, the global temperature and ozone observations at whole heights and in both groups were processed into zonal mean results, covering latitudes from 50°S to 50°N with a resolution of 5°. At a fixed latitude and height, the following equation proposed by Xu et al. (2007) is used to extract the tide from the zonal mean temperature in a 60-day window:

$$\frac{1}{2\pi}\int_0^{2\pi} T(t_{LT},\lambda)d\lambda = \bar{T} + \eta(t - t_0) + \sum_{n=1}^{N} A_n cos(n\omega t_{LT}) + \sum_{n=1}^{N} B_n sin(n\omega t_{LT}) \qquad (2)$$

where ω = 2π/24(hour), t_{LT} is the local time, λ is longitude in radians. $\bar{T}$is the 60-day window average of the zonal mean temperature. η describes the linear trend variation in the window. t is the day of the window and t_0 is the center day of the window. The third and fourth term of the right section of the equation denotes the superimposed harmonic signals by four periods migrating tides, including diurnal tide (DW1), semidiurnal tide (SW2), terdiurnal tide (TW3), and 6-h tide (QW4). N in the third term represents four signals and n denotes each signal. The amplitude and phase of each migrating tide are retrieved using $\sqrt{A_n^2 + B_n^2}$ and $arctan(B_n/A_n)$, respectively. The overlapping analyses are obtained by sliding the 60-day window forward in 1-day intervals to obtain the daily values of the wave characteristics. The details of the methods used for data processing and tide extraction could refer to Xu et al. (2007, 2009) and Liu et al. (2024a).

The method for extracting tidal components from ozone heating rates follows Equation 4 in Xu et al. (2010). The methods for tidal extraction from MERRA-2 and SD-WACCM-X differ from those used for SABER due to differences in data structure. Unlike SABER, both MERRA-2 and SD-WACCM-X provide spatially uniform data with a 3-hour temporal resolution. As a result, a two-dimensional Fast Fourier Transform (2D-FFT) is directly applied to extract daily DW1 amplitudes and phases of temperature, water vapor heating rate, and temperature tendency due to moist processes. For the further analysis, the Hough mode decomposition is applied to the DW1. The program is retrieved from https://github.com/masaru-kogure/Hough_Function. As in Sakazaki (2013), DW1 in the stratosphere can be reasonably well represented by a superposition of only a few (~ 4) Hough modes. Here the (1, -2), (1, -1), (1, 1) and (1, 2) mode are used. The monthly mean temperature DW1 amplitudes obtained from SABER, MERRA-2 and SD-WACCM-X are calculated. Due to the observational gap of SABER, the Generalized Lomb-Scargle Periodogram (from PyAstronomy) is applied to fill the missing data of ozone heating rate. A low-pass Butterworth filter of 3rd order with a cut-off period of 13 months (≈ 0.077 cycles month^{-1}) is applied to reveal the DW1 QBO variations (temperature, ozone heating and so on).

3 Result

3.1 DW1 amplitude response to QBO disruption events

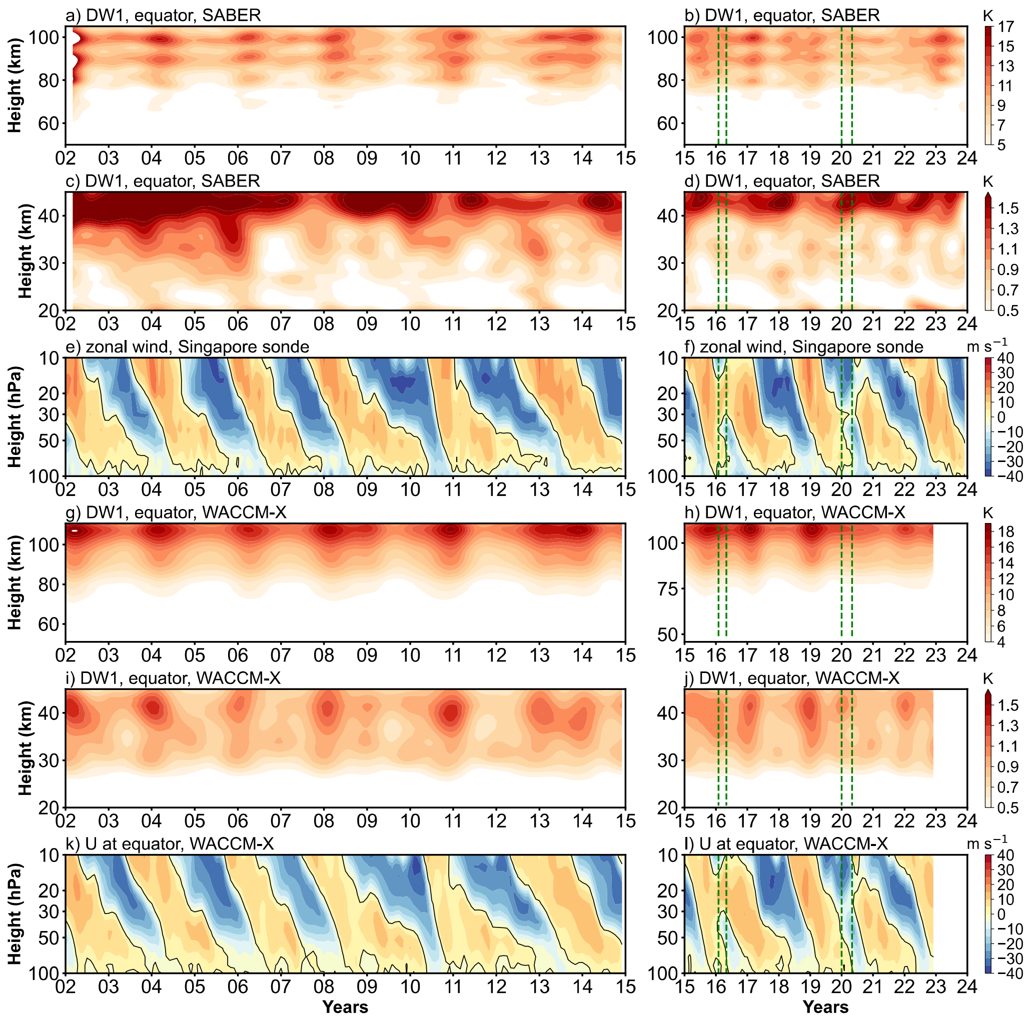

Figure 1. (a, b) Low-pass filtered amplitudes (periods longer than 13 months) of the migrating diurnal tide (DW1; monthly mean, in K) as a function of altitude in the mesosphere and lower thermosphere (MLT) and time (2002–2023), derived from SABER/TIMED temperature observations. (c, d) Same as (a, b) but for the stratosphere. (e, f) Zonal wind at the stratospheric equator from Singapore sonde. (g–i) Similar to (a–f), but based on SD-WACCM-X simulations. Vertical green dashed lines indicate the QBO disruption periods in 2015/16 (February–May 2016) and 2019/20 (January–May 2020).

Figure 1 presents the amplitude of DW1 after low-pass filtering and the zonal wind observed by the Singapore sonde. Only amplitude components longer than 13 months are retained. In the stratosphere, the zonal wind shows alternating downward propagating westerly wind (positive value in Figure 1e and 1f) and easterly wind (negative value in Figure 1e and 1f). Each westerly and easterly transition can be called a QBO cycle. In the stratosphere (Figure 1c and 1d), below 40 km, the amplitude of DW1 also shows Quasi-Biennial variability. Above 40 km, the variation is more complex. This feature will be discussed later. In the MLT region (Figure 1a and 1b), the low-pass filtering results of DW1 at the equator exhibit Quasi-Biennial variability, with amplitude peaks observed around 90 and 100 km. Comparing the DW1 amplitudes in MLT with the zonal wind, the result reveals that the variations in DW1 amplitude correspond to the zonal wind between 20 and 30 hPa. The amplitude of DW1 is stronger during the QBO westerly wind phase than during the QBO easterly wind phase. This result is consistent with Garcia (2023) that the wind fields of QBO at altitudes below 27 km are clearly correlated with the DW1 amplitude. Accordingly, in this work, the zonal wind between 20 and 30 hPa is used as the criterion for defining the QBO for DW1.

During February–May 2016 and January–May 2020, two QBO disruption events occurred (Wang et al., 2023). As shown in Figure 1f, the phenomenon ranges from 40 to 15 hPa in 2016 and from 40 to 20 hPa in 2020, which is consistent with previous work (Anstey et al., 2021; Newman et al., 2016). Notably, the disruption region coincides with the QBO criterion altitude for DW1. To evaluate how the DW1 exhibits response to the events, the corresponding time intervals are highlighted with vertical green dashed lines. In the stratosphere (Figure 1d), within the disruption periods, amplitude enhancements are observed below 40 km compared to other QBO easterly phases. Similarly, in the MLT region, the DW1 amplitudes show responses to these events (Figure 1b). As shown in Figures 1a and 1b, DW1 amplitudes above 70 km are stronger during these disruption events than during other QBO easterly phases, though they remain weaker than those observed during the QBO westerly phase. This enhancement is particularly evident around 90 and 100 km.

SD-WACCM-X simulations reproduce the SABER observations of DW1 remarkably well in response to QBO disruptions. In Figures 1a, 1b, 1f, and 1g, both datasets show enhanced amplitudes during the February–May 2016 and January–May 2020 events. The difference arises in vertical structure and magnitude. Above 70 km, SABER exhibits three distinct DW1 peaks near 80, 90, and 100 km, whereas SD-WACCM-X shows a single peak at approximately 108 km. In the stratosphere above 40 km, both model and observations peak at similar altitudes, but the simulated amplitudes remain weaker than SABER result. Below 40 km, the model captures the QBO-modulated DW1 seen in Figures 1c, 1d, 1i, and 1j. These discrepancies likely stem from the MERRA-2 nudging applied up to ~50 km in SD-WACCM-X. In this nudged region, DW1 comprises both propagating and non-propagating components (Garcia, 2023; Chapman & Lindzen, 1970). Sakazaki et al. (2018) showed that MERRA-2 may underestimate the contribution of the non-propagation mode of DW1 (Figure 4 in that work). This feature may explain why the amplitude of DW1 is lower than that in SABER and the complex variation of SABER above 40 km.

To assess the DW1 response to QBO disruption events over a broad latitude range, the differences between QBO disruption and regular QBO easterly and westerly are calculated. The DW1 amplitudes used is the result after 13 months low-pass filtering. Since the DW1 amplitudes typically peak between February and April each year (e.g., Xu et al., 2009; Mukhtarov et al., 2009; Garcia, 2023), only the amplitudes during these three months are considered. The classification method for different QBO phases is as follows. Regular QBO phases were classified as following method. QBO westerly phase (QBOW): February–April zonal wind at 20 hPa is continuously westerly, or zonal wind at 30 hPa is westerly while 20 hPa undergoes an easterly-to-westerly transition. Easterly phase (QBOE): any remaining cases. The selection of regular QBO phases is limited to data from 2002 to 2014, as QBO disruption events occurred after 2015. Additionally, since observations in 2002 are mainly available from March to April, data from this year are excluded. The years 2004, 2006, 2008, 2011, 2013, and 2014 are classified as QBOW; 2003, 2005, 2007, 2009, 2010, and 2012 as QBOE. For each phase, all filtered amplitudes across the selected months are averaged, while processing 2016 and 2020 separately. This approach enables a direct comparison of DW1 amplitude anomalies in both latitude and altitude between disruption and regular QBO conditions.

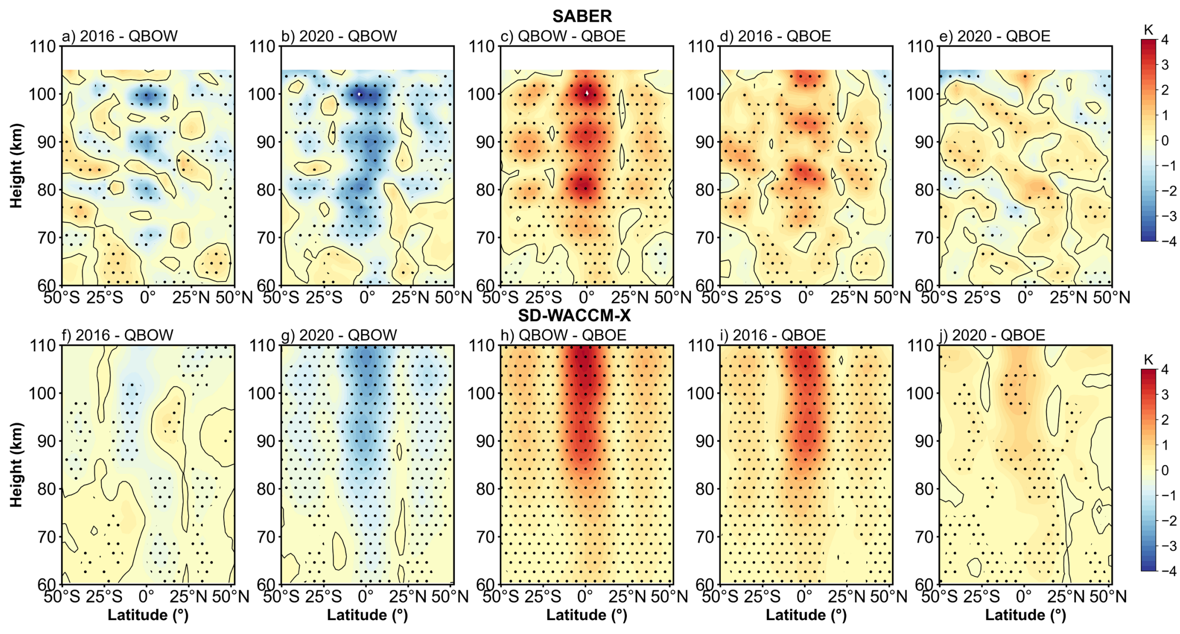

Figure 2. Amplitude differences of the DW1 after low-pass filtering between different QBO phases in the mesosphere and lower thermosphere (MLT) as a function of latitude and altitude. The difference is based on the average from February to April. (a-e) are corresponding to the difference from the 2016 disruption event minus QBO westerly phases (2016-QBOW), 2020 disruption event minus QBO westerly (2020-QBOW), QBO westerly minus QBO easterly (QBOW-QBOE), 2016 disruption event minus QBO

easterly (2016-QBOE) and 2020 disruption event minus QBO easterly (2020-QBOE). (f-j) is similar to (a-e) but for SD-WACCM-X simulation result. The black lines indicate the zero lines. The dotted areas indicate the difference that are significant at the 95% confidence level.

Figure 2 gives the difference in DW1 amplitudes during various QBO phases in the MLT region. The significance of the differences was assessed using Welch's t-test, and values exceeding the 95 % confidence threshold are highlighted by dotted. The five columns correspond to the 2016 disruption event minus QBO westerly (2016-QBOW), 2020 disruption event minus QBO westerly (2020-QBOW), QBO westerly minus QBO easterly (QBOW-QBOE), 2016 disruption event minus QBO easterly (2016-QBOE) and 2020 disruption event minus QBO easterly (2020-QBOE), respectively. The relative change between different QBO phases is also calculated (e.g., $\frac{\mathrm{QBOW-QBOE}}{\mathrm{QBOE}}$, and so on). The comparison between QBOW and QBOE (Figure 2c) reveals that DW1 amplitudes are significantly larger during QBOW, particularly at the equator and around 30°N/S above ~75 km. The enhancements reach ~2.79 K (~34.5 %) at the equator and ~0.79 K (~20.6 %) at 30°N/S, with peak values as high as ~3.30 K (~38.5 %) and ~1.19 K (~31.7 %) at respective latitudes. During the 2016 disruption (Figures 2a, 2d), DW1 amplitudes lie between QBOE and QBOW values. The clear enhancement could be found from 75 km to 105 km. The pattern in 2016–QBOE closely resembles that of QBOW–QBOE, although the equatorial peaks appear at slightly higher altitudes. The enhancements reach ~1.56 K (~20.5 %) at the equator and ~0.54 K (~14.4 %) at 30°N/S. The peak enhancements relative to QBOE reach ~2.40 K (~26.5 %) at the equator and ~0.87 K (~29.5 %) at 30°N/S. Compared to QBOW, however, the equatorial difference drops to –2.28 K (–18.8 %). In contrast, the 2020 disruption event shows weaker amplitude increases relative to QBOE (Figures 2b, 2e). The clear enhancement occurs from 75 km to 90 km. The increment reach ~0.50 K (~6.0 %) at the equator and ~0.26 K (~7.7 %) at 30°N/S, with a peak enhancement of only ~0.91 K (~11.6 %) at the equator and ~0.31 K (~14.2 %) at 30°N/S. These values are considerably lower than those observed during the 2016 event or the typical QBOW enhancement. The SD-WACCM-X model reproduces the general features described above (Figures 2f–2j), though the vertical structure of the simulated amplitudes differs slightly from observations.

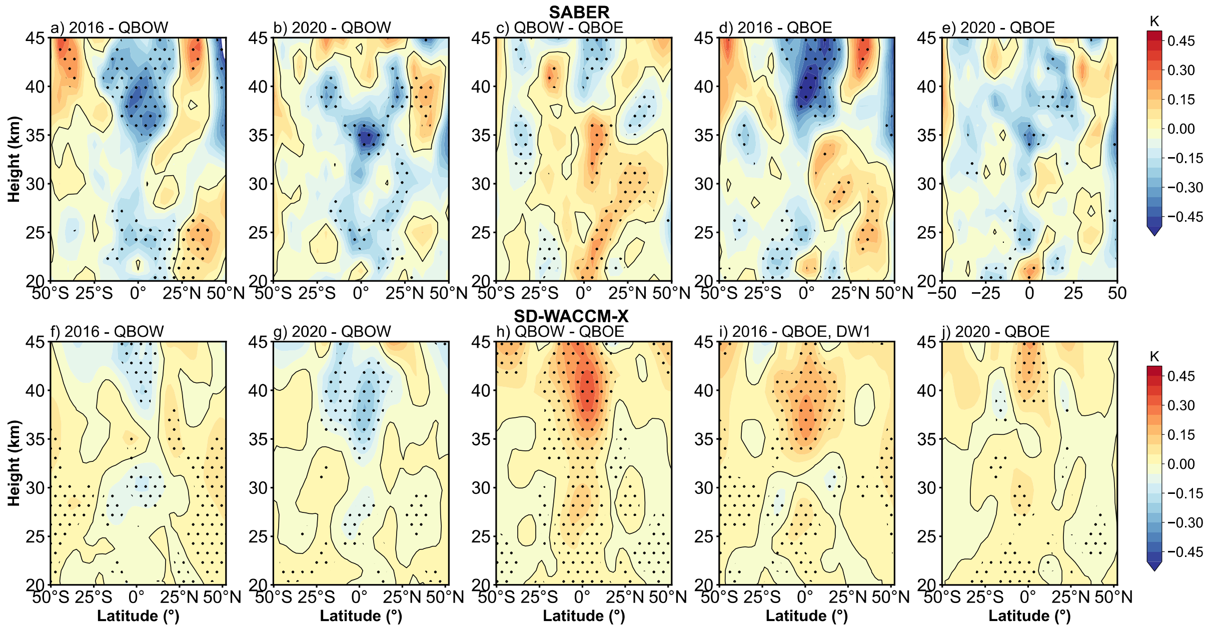

Figure 3. Similar to figure 2 but in stratosphere. (a-e) give the difference result derived from SABER. (f-g) give the difference result derived from SD-WACCM-X.

Figure 3 compares the stratospheric DW1 amplitude differences derived from the SABER dataset and SD-WACCM-X simulations. The enhancement pattern resembles that seen in the MLT region but is confined to tropical latitudes. Because SABER exhibits complex variability above 40 km, the analysis is restricted to altitudes below that level. As shown in Figure 3c, the DW1 amplitudes during QBOW exceed those during the QBOE by ~0.21 K (~37.9 %) at around 20-25 and 30-35 km. In SD-WACCM-X result (Figure 3h), the positive peaks are found at 25-30 km and 35-40 km, which is ~0.21 K (~27.4 %). The amplitudes during the disruption events are much weaker relative to that during QBOW phases shown in both datasets (Figure 3a, 3b, 3f and 3g). Compared to the QBOE, the strengthening during the 2016 QBO disruption event occurs at approximately 30–35 km in SABER (Figure 3d) and 35-45 km in SD-WACCM-X (Figure 3i), which is ~0.15 K (~21.8 %) and 0.20 K (~23.9 %), respectively. During the 2020 event, the amplitudes are comparable relative to the QBOE (Figure 3e and 3j).

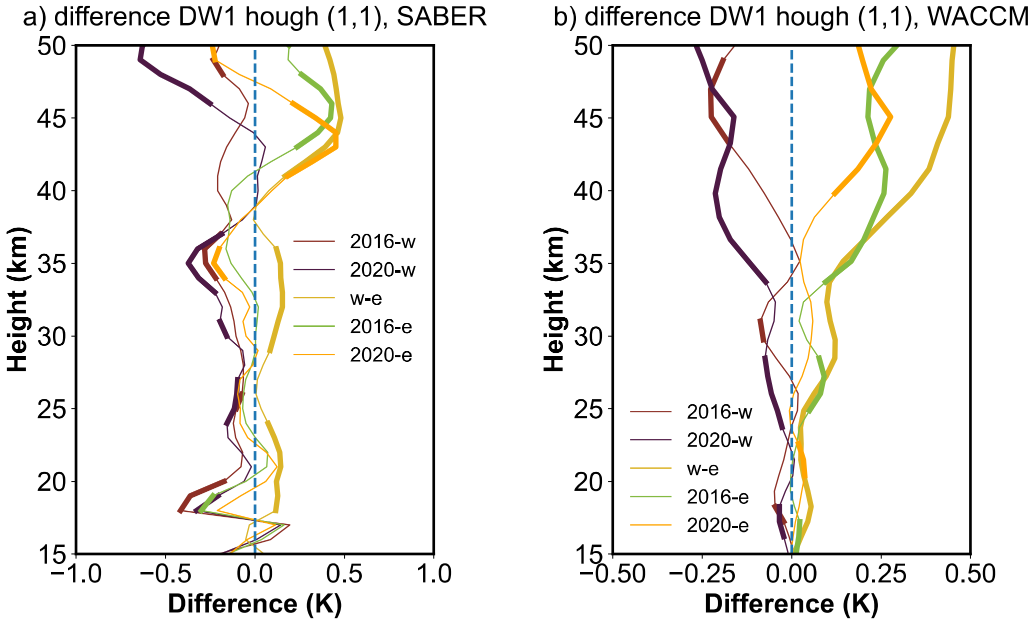

Figure 4. Amplitude differences profiles of the DW1 (1, 1) mode after low-pass filtering between different QBO phases in the stratosphere like Figure 2. (a) give the difference result derived from SABER. (b) give the difference result derived from SD-WACCM-X. The bold lines indicate the difference that are significant at the 95% confidence level.

Figure S2 presents the low-pass time series of the equatorial DW1 amplitude and the (1,1) mode amplitude at 95 km, showing that the (1,1) mode closely follows the equatorial DW1 amplitude. In the stratosphere, however, the superposition of propagating tides and trapped modes complicates the interpretation. To separate these contributions, Figure S1 compares the amplitudes of the (1,1) and (1, –2) modes under different QBO phases. The trapped mode is dominant below 60 km, while the (1,1) mode is relatively weaker. A clear distinction between QBOW and QBOE is evident in the (1,1) mode (Fig. S1a), whereas the (1, –2) mode shows little difference between the phases. Together, Figures S1 and S2 indicate that the (1,1) mode captures nearly all of the QBO-related variability in the MLT region, motivating a closer examination of this mode in the stratosphere. Figure 4 shows the vertical profiles of amplitude differences in the DW1 (1,1) mode between QBO phases after low-pass filtering. The bold lines denote differences significant at the 95% confidence level. In SABER observations (Fig. 4a), amplitudes during QBOW exceed those in QBOE throughout 20–45 km. During the 2016 and 2020 events, amplitudes remain close to QBOE between 20–40 km but become stronger above 40 km, with maximum differences of ~0.36 K (~36 %), ~0.21 K (~21 %), and ~0.18 K (~17 %) for QBOW–QBOE, 2016 – QBOE, and 2020–QBOE, respectively. WACCM-X simulations (Fig. 4b) reproduce a similar vertical pattern: during the disruption events, amplitudes lie between QBOE and QBOW values in the 20–50 km region.

3.2 DW1 phases response to QBO disruption events

In this section, whether the DW1 phases and wavelengths respond to QBO disruptions will be analysed. As discussed above, the DW1 QBO variability is mainly in (1, 1) mode. Hence, the phase of (1, 1) mode is focused. As noted previously, the pronounced DW1 amplitude observed from February to April renders the phase during this period an important variable. Hence, the statistic is based on these periods. Due to the phase values change cyclically (e.g., it jumps from pi to -pi), causing the overestimation of the standard deviation. We apply the method following. Calculate averages and standard devotion (or error) of sine and cosine Fourier components first, and then calculate the average phase and its confidential interval using the error propagation. The mean value and its 95% confidential interval in different QBO phases (listed in section 3.1) are calculated. The statistical results for the phases in 2016 and 2020 are calculated separately.

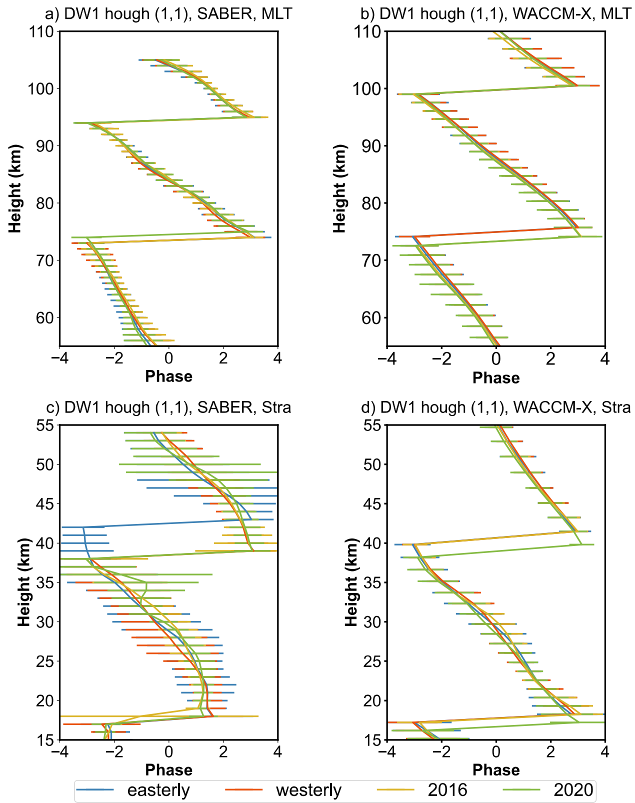

Figure 5. The DW1 (1, 1) mode vertical phase structure in mesosphere and lower thermosphere (MLT) and stratosphere averaged from February to April during QBO westerly phase (orange), QBO easterly phase (blue), 2016 QBO disruption event (yellow) and 2020 QBO disruption event (green). (a, c) give the SABER observation result. (b, d) give the WACCM-X simulations. The error bar denotes the 95% confidential interval of the phases for each height.

Figure 5 illustrate the vertical phase structure of DW1 (1, 1) mode in the mesosphere and lower thermosphere (MLT) and stratospheric regions, respectively, averaged over the February–April period. The results are presented for various QBO phases at different latitudes, based on data from (a, c) SABER and (b, d) SD-WACCM-X. Error bars indicate the 95% confidential interval of the phase average. The lines represent different QBO phases and events: QBO westerly phase (orange), QBO easterly phase (blue), the 2016 QBO disruption event (yellow), and the 2020 QBO disruption event (green).

In the MLT region (Figure 5a and 5b), the vertical phase profiles exhibit minimal differences across the QBO westerly, easterly and 2016 phases. The structures are nearly identical in both the simulations and observations, with two phase peaks (approximately π rad) consistently present. The peak altitudes remain almost unchanged among the different QBO phases, suggesting a limited phase response to QBO disruption events in the MLT region. During the 2020 event, the phase peaks at around 75 km is higher than that during other QBO phases in SABER and lower in that in WACCM-X.

The DW1 vertical phase structures in the stratosphere region are given in Figure 5c and 5d. In SABER observations, there is clear difference between QBOW and QBOE. The phase peaks (at around 40 km) during the QBOW locate lower than QBOE about 3 km. During the QBO disruption events, the phase structure is similar to that during the QBOW. From WACCM-X simulations, the feature is similar to the pattern in MLT (Figure 5b). During 2020 disruption event, the phase reach peaks lower than other QBO phases about 1 km.

The phase peaks described above (~π rad) are used to calculate the DW1 wavelengths in both the stratosphere and MLT regions. The altitude difference between the two peaks is taken as the wavelength, following Liu et al. (2021). The statistical results of DW1 (1, 1) mode wavelengths under different QBO phases are summarized in Table 1, which lists the mean values and standard deviations at various altitudes. In the MLT region, the mean wavelengths are ~21 km in the SABER dataset and ~25 km in the SD-WACCM-X dataset. The wavelengths during QBO disruption events are comparable to those during the QBO westerly and easterly phases, a feature also captured in the SD-WACCM-X simulations. In the mesosphere, the mean wavelengths are ~34 km in SD-WACCM-X and ~33 km in SABER. In this region, there are clear differences between QBOW and QBOE. The QBOE wavelength is shorter than QBOW about 2 km. In the stratosphere, the QBOE wavelength is longer than QBOW about 2 km. The wavelengths during the QBO disruptions are close to that during QBOW.

Table 1. The comparison of mean (left of the slash) and standard deviations (right of the slash) of DW1 (1, 1) mode wavelengths (in km) revealed by SD-WACCM-X and SABER from 15 km to 105 km between QBO westerly phase, easterly phase, 2016 disruption event and 2020 disruption event calculated from February to April.

Data	SD-WACCM-X			SABER		
altitude	~15 km – ~ 40 km	~40 km – ~ 75 km	~75 km – ~105 km	~15 km – ~ 40 km	~40 km – ~ 75 km	~75 km – ~105 km
Westerly	22.97/1.49	34.47/1.79	25.10/1.84	21.81/1.44	33.12/1.78	21.29/1.04

Easterly	22.51/1.73	34.42/2.15	25.60/2.20	24.46/1.99	30.84/2.35	20.56/1.30
2016	22.56/1/33	33.26/1.58	25.58/2.03	21.48/2.31	33.32/2.10	21.28/0.85
2020	22.71/1.87	33.80/2.68	26.27/2.41	21.08/1.77	34.24/1.46	20.39/1.35

4 Discussion

4.1 Tidal heating

The influence of QBO disruption events on DW1 can be traced back to its excitation mechanisms. The excitation sources of DW1 can be broadly classified into three categories: (1) solar radiation in the near-infrared (IR) absorbed by tropospheric H_2O, (2) solar radiation in the ultraviolet (UV) absorbed by stratospheric and lower mesospheric O_3, and (3) solar radiation absorbed by O_2 in the Schumann–Runge bands and continuum (Hagan, 1996). Additionally, Kogure and Liu (2021) suggested the role of latent heating in modulating DW1.

It is worth noting that the timing of the 2016 QBO disruption event coincides with the phase of the extreme El Niño (e.g., Santoso et al., 2017; Hu and Fedorov, 2017). El Niño itself could modulate the DW1 (Kogure and Liu, 2021). The contribution of water vapor and latent heating should be also paid attention.

During the 2016 QBO disruption, which coincided with the strong 2015/2016 El Niño, the two phenomena jointly modulated the DW1 heating sources. El Niño enhances moisture anomalies that increased with altitude, culminating in pronounced positive signals in the upper troposphere and lower stratosphere (UTLS) (Johnston et al., 2022). In contrast, the occurrence of 2016 QBO disruption introduces a shear transition from westerly to easterly near 40 hPa, which strengthens tropical upwelling and lowers cold-point temperatures. This dynamical response injects H_2O-poor air into the lower stratosphere, partially offsetting the El Niño–driven moistening. The water vapor concentrations are still above the climatological seasonal cycle under the modulation of these two phenomena (Diallo et al., 2018). Unlike 2016, the 2020 disruption produces only weak lower-stratospheric dehydration (~2–3 %) because enhanced upwelling and cold-point cooling are suppressed. Instead, anomalously warm tropopause temperatures associated with Australian wildfire smoke facilitates significant moistening of the lower stratosphere (Diallo et al., 2022).

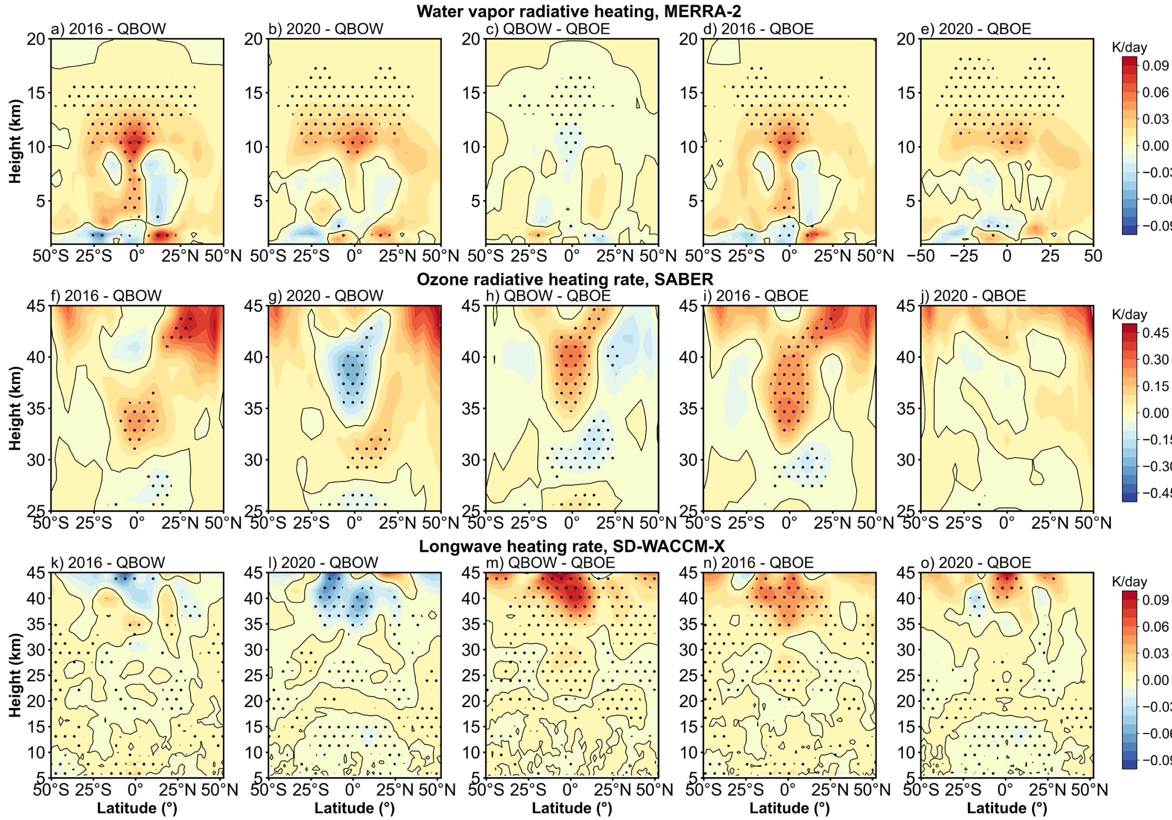

Figure 6. As in Figure 2 and Figure 3, but the difference of amplitude in DW1 component (after low-filtering) of (a-e) water vapor heating rate DW1 component from MERRA-2, (f-j) ozone heating rate DW1 component from SABER and (k-o) longwave heating rate from SD-WACCM-X. The dotted areas indicate the difference that are significant at the 95% confidence level.

Figure 6 presents the difference of amplitude in the DW1 component of water vapor radiative heating rate, ozone radiative heating rate, and longwave heating rate. The calculation method is consistent with the method given in Section 3.1. During QBOE and QBOW, the DW1 component of water vapor heating remains nearly unchanged (Figure 6c). However, during the 2016 QBO disruption (Figures 6a, 6d), a notable enhancement in water vapor heating appears between 10–13 km altitude around equator. The difference between 2016 and QBOE is ~0.02 K day^{-1} with increases of ~2.5% relative to QBOW. The difference between 2016 and QBOW is 0.03 K day^{-1} with increases of ~3.7% relative to QBOW. A similar pattern is seen during the 2020 QBO disruption event (Figures 6b and 6e). The relative changes of regional average rise by ~1.2 % compared to QBOW and ~2.3 % compared to QBOE.

Figures 6f–6j reveal that the largest QBO-related differences in the DW1 component of ozone heating occur near the equator between 30 and 45 km. In QBOW, ozone heating rates between 35 and 45 km exceed those in QBOE by ~2.1 % (Figure 6h). During the 2016 QBO disruption event (Figures 6f and 6i), ozone radiative heating rates are ~3.6 % larger than those in the

QBOW between 30 and 35 km and ~2.9 % larger than those in the QBOE within the 30–40 km range. In contrast, during the 2020 disruption event (Figures 6g and 6j), the ozone heating rate is comparable to that of the easterly phase and lower than that of the westerly phase in the 35–45 km altitude range.

In the SD-WACCM-X simulation, the longwave heating rate accounts for the effects of three major absorbers: H_2O, CO_2, and O_3 (Neale et al., 2010). This parameter could be used to verify the effect of the water vapor and ozone radiative heating. The DW1 component of the longwave heating rate from SD-WACCM-X is shown in Figures 6k–6o. The heating rate difference between the QBOW and QBOE reveals a positive peak at 40 km near the equator, with no significant difference at the equatorial tropopause (Figure 6m). The feature corresponds to the observed pattern (Figures 6c and 6h). In the 2016 disruption case, the simulated equatorial heating rate exhibits positive peaks around 35 km and 15 km (not significant), aligning well with observations in terms of altitude (Figure 6k and 6n). In the 2020 disruption case, the simulation (Figure 6l and 6o) agrees with the observed stratospheric heating features (Figures 6g and 6j). However, at around 15 km, the simulation shows negative peaks near the tropopause, whereas the observations indicate positive peaks (Figures 6b and 6e). As longwave heating incorporates contributions from multiple absorbers, the discrepancies may be attributed to the influence of other constituents.

As discussed above, the (1,1) Hough mode captures nearly all QBO-related variability in the MLT. Accordingly, the (1,1) component of the ozone heating rate are extracted for diagnosis. Numerous studies have noted that the vertical thickness of ozone heating (~40 km) is large compared with the relatively short vertical wavelength of the DW1, implying weak projection onto the (1,1) and thus limited excitation efficiency (e.g., Chapman and Lindzen, 1970; Hagan, 1999; Garcia, 2023). Studies with GSWM and the Tide Mean Assimilation Technique (TAMT) further indicate that DW1 forced by ozone heating tends to be out of phase with DW1 forced by water-vapor heating, reducing the amplitudes (Hagan, 1996; Ortland et al., 2017). Consistent with this mechanism, MLS observations show a pronounced depression of the tropical diurnal tide near 1.0 hPa (~49.5 km; Wu et al., 1998), which may attribute to interference between the upward-propagating (1,1) tide and a locally forced component from ozone heating. Figure 7 compares DW1 (1,1) temperature and ozone heating rate between different QBO phases and shows suppressed (1,1) amplitudes feature around ~50 km, while ozone heating peaks slightly below this level. This feature aligns with the MLS evidence. Therefore, the ozone may not play positive role for the DW1 (1, 1) mode. Whether the ozone heating modulated DW1 (1, 1) mode, there needs more detailed investigation like model simulation from Kogure et al. (2023).

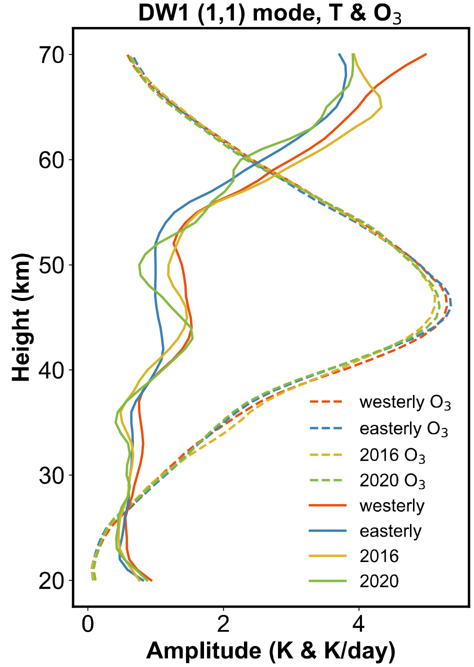

Figure 7. The comparison between temperature and heating rate of the DW1 (1, 1) mode between different QBO phases and their differences.

The DW1 (1,1) mode is primarily excited by water-vapor heating (Forbes and Garrett, 1978). Figure 8 presents the water vapor heating rate profiles of the DW1 (1,1) mode for different QBO phases and their differences. The heating rate exhibits large values in the troposphere, extending up to ~10 km. The average magnitude could reach ~0.62 K day^{-1}. During the 2016 QBO disruption event (Fig. 8b), the maximum difference occurs at 10.5 km, reaching 0.043 K day^{-1}, which represents an ~8 % increase relative to QBOE. However, the DW1 amplitude varied by ~20.5 % compared to QBOE, indicating that water-vapor heating accounts for only ~39 % of the observed amplitude difference. This feature suggests that additional mechanisms must be involved. A similar enhancement of water-vapor heating is observed during the 2020 event, with the largest difference again at 10.5 km (~0.026 K day^{-1}), corresponding to an ~5 % increase relative to QBOE.

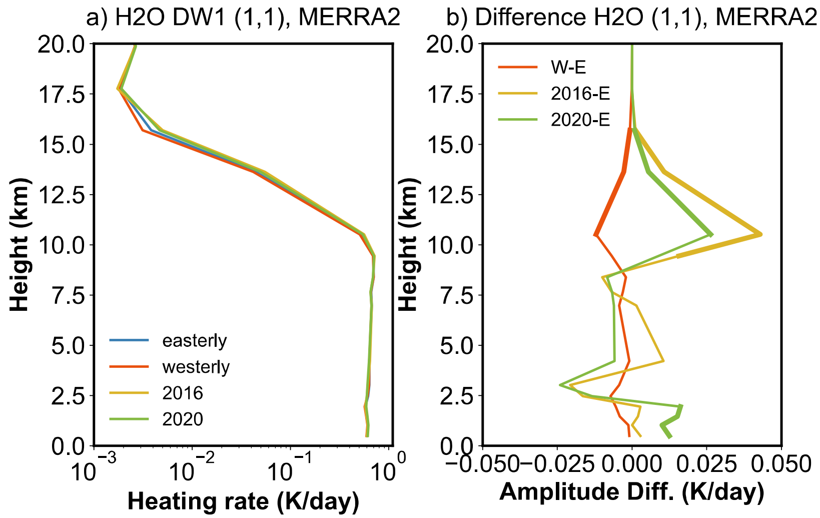

Figure 8. Heating rate profiles of the DW1 (1, 1) mode between different QBO phases and their differences. (a, b) give the water vapor heating profile and its difference derived from MERRA2. The bold lines indicate the difference that are significant at the 95% confidence level.

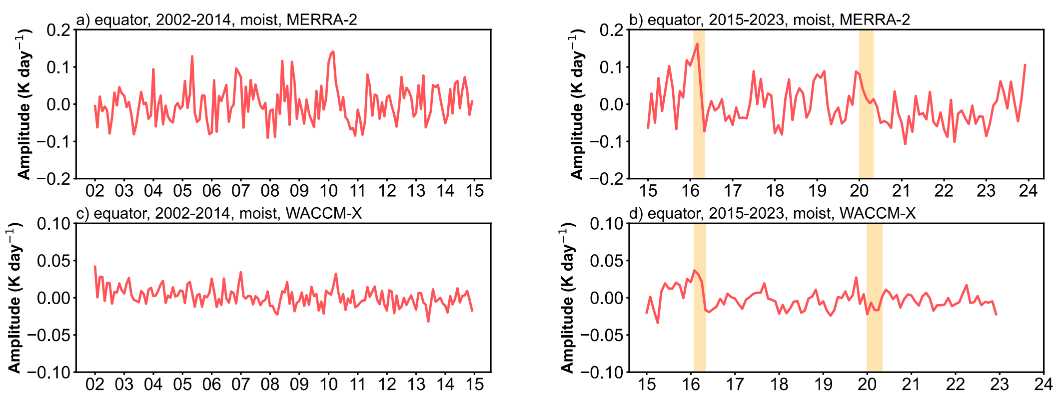

Figure 9. (a, b) The deseasonalized time series of DW1 amplitudes of latent heating rate (K day^{-1}) at equator averaged from 800 hPa to 200 hPa derived from MERRA-2. (c-d) is as in (a-b) but from SD-WACCM-X. The orange-filled areas represent two QBO disruption events.

Figure 9 shows the deseasonalized time series of the DW1 component of latent heating rate (K day^{-1}) at the equator, averaged from 800 hPa to 200 hPa. In this tropospheric layer, the latent-heating signal shows less differences between QBOW and QBOE phases. Therefore, deseasonalization is directly applied to the full time series without separating the two QBO states. In MERRA-2 and SD-WACCM-X, the anomaly peaks reach 0.162 K day^{-1} and 0.037 K day^{-1}, respectively, which correspond to increases of about ~32 % and ~25 % above their climatological means (0.50 K day^{-1} and 0.15 K day^{-1}). When averaged over the February-April in 2016, the anomalies remain elevated at 0.11 K day^{-1} (~22 %) in MERRA-2 and 0.03 K day^{-1} (~19.2 %) in SD-WACCM-X. In contrast, during the 2020 QBO disruption event, the amplitudes in both MERRA-2 and SD-

WACCM-X remain closer to the climatological means, with deviations of 0.018 K day^{-1} and -0.013 K day^{-1}, respectively. These results suggest that latent heating may contribute to the amplification of DW1 amplitudes during the 2016 QBO disruption event but show little effect during the 2020 event.

4.2 Tidal propagation

As discussed in Forbes and Vincent (1989), the (1,1) mode is dissipated more in the easterly wind than in the westerly wind. Zonal winds distort the tidal expansion functions such that they are amplified and broadened in the winter hemisphere (U > 0) but are considerably diminished under summer conditions. During the 2016 QBO disruption, the westerly wind layer is unusually thick in stratosphere, though still weaker than in the normal QBOW. Under these conditions, the background wind tend to enhance tidal amplitudes. However, the thinner westerly layer compared with the normal QBOW phase likely contribute to somewhat weaker amplitudes. In contrast, during the 2020 event, the westerly wind layer is extremely shallow, essentially indistinguishable from the easterly phase, so the background wind exerts little or no amplifying effect on tides compare to QBOE.

In addition to zonal-mean wind effects, latitudinal shear of zonal wind in the subtropical mesosphere can modulate the seasonal variability of the (1,1) mode (McLandress, 2002b; Mayr and Mengel, 2005; Sakazaki et al., 2013; Kogure et al., 2021; Siddiqui et al., 2022). Large values of $|\partial u/\partial y|$ at some height, are equivalent in some sense to faster rotation, which restricts the latitudinal band or waveguide where the diurnal tide can propagate vertically, thus reducing the tidal amplitude above by removing tidal energy at that altitude (McLandress, 2002b; Siddiqui et al., 2022). The wind shear at 18°N/S are typical indicators (Kogure et al., 2021).

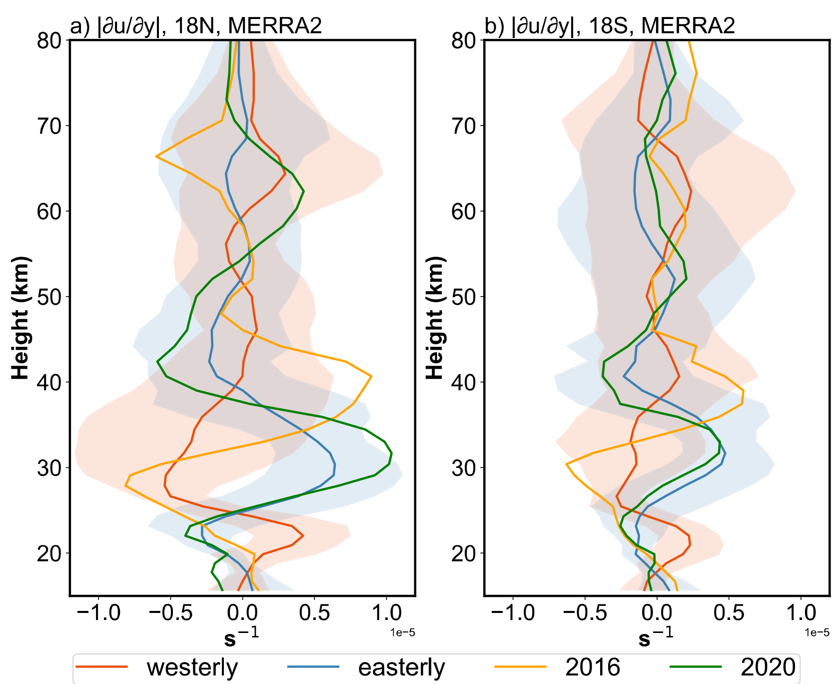

Figure 10. The |∂u/∂y| profiles after deseasonalized between different QBO phases at (a) 18°N and (b) 18°S. The colourful shaded areas denote one standard deviation of the phases for each height.

The monthly |∂u/∂y| at 18°N/S is calculated, deseasonalized, and classified following the method described in Section 3.1. The |∂u/∂y| profiles for different QBO phases are shown in Figure 10. During QBOW, a pronounced negative anomaly appears near 30 km, whereas during QBOE a strong positive anomaly is evident at the same altitude. During the 2016 disruption event, the |∂u/∂y| profile at 18°N exhibits a structure broadly similar to that of QBOW. However, from 35 to 45 km it shows large positive values, a feature not observed in other QBO phases. The |∂u/∂y| profile at 18°S displays a similar vertical structure but with smaller amplitudes. Based on this structure, the tide may be amplified near 30 km and subsequently damped near 40 km, which could partly explain why the tidal amplitudes during the 2016 disruption do not reach those observed in QBOW. In contrast, the |∂u/∂y| during the 2020 disruption event closely resembles the QBOE structure, suggesting that the tidal propagation background was similar to QBOE conditions.

4.3 Tide-gravity wave interaction

The mesospheric diurnal tides are also affected by the interaction with GWs (Liu and Hagan, 1998; Mayr et al., 1998; Mclandress, 2002a; Li et al., 2009; Lu et al., 2012; Yang et al., 2018; Stober et al., 2021; Cen et al., 2022). It could greatly modulate tidal amplitude and phase (Liu and Hagan, 1998; Lu et al., 2009; Li et al., 2009; Wang et al., 2024). To quantify the GW forcing on the DW1, the method of Yang et al. (2018) and Cen et al. (2022) are applied. The equation is:

$$\mathrm{GW}_{\mathrm{forcing}} = \mathrm{GW}_{\mathrm{drag}} \cdot \cos\left(\omega \cdot \left(\phi_{\mathrm{GW}} - (\phi_T - 6)\right)\right) \quad (3)$$

Where the $\mathrm{GW}_{\mathrm{drag}}$ is the DW1 amplitude of GW drag, ω is the $24/2\pi$, ϕ_{GW} is the DW1 phase of GW drag while ϕ_T is DW1 amplitude of temperature.

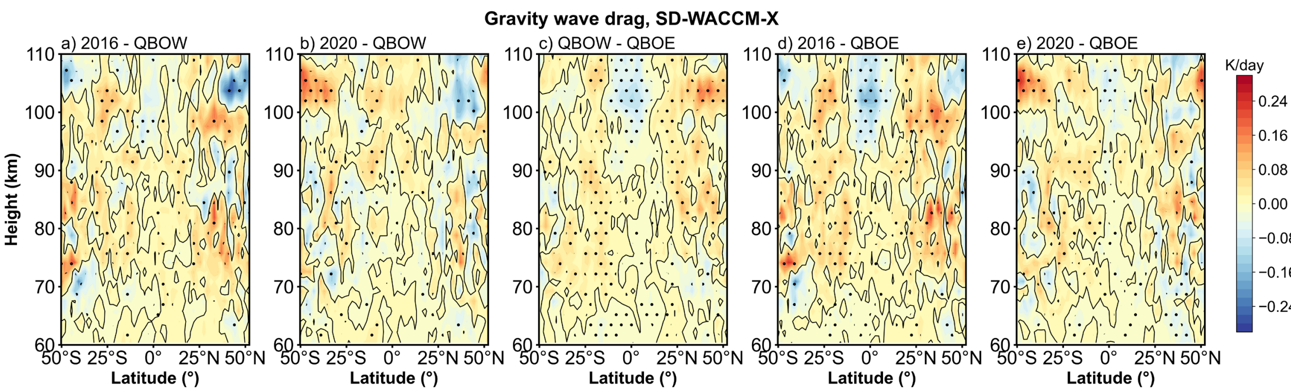

Figure 11. Similar to figure 2 but the difference of gravity wave forcing. (a-e) give the difference result derived from SD-WACCM-X.

After calculating the GW forcing, the classification method in Section 3.1 is applied. As shown in Figure S3, GW tend to damp the DW1 amplitude at nearly all latitude above 105 km. Below ~105 km, the GWs tend to damp the DW1 amplitude at equator and strengthen the DW1 amplitude at subtropical. There are differences in the amplitude of gravity wave drag between different QBO phases. Figure 11 shows the differences in GW forcing between QBO phases, with dots indicating regions exceeding the 95% significance level. During QBOW (Fig. 11c), the equatorial damping and subtropical enhancement are stronger than during QBOE. During the 2016 QBO disruption event, the pattern closely resembles the QBOW–QBOE difference but with larger magnitude than QBOW (Fig. 11a). During the 2020 disruption event, the GW drag is close to QBOW conditions and is stronger than in QBOE. These results suggest that GW forcing exerts a significant influence on the modulation of DW1 amplitudes across QBO phases and disruption events.

5 Summary

In this work, the response of global DW1 amplitudes and phases during QBO disruption events is investigated using SABER observation, MERRA-2 dataset and SD-WACCM-X simulation results from 2002 to 2023. Additionally, the underlying mechanisms during the event is explored. The findings are summarized as follows:

(1) There is clear difference in (1, 1) mode vertical phase structure and wavelengths between QBO westerly phases and easterly phases. The DW1 (1, 1) mode vertical phase structure and wavelengths during these two QBO disruption events is similar to that during QBO westerly phases.

(2) In the 2016 QBO disruption event, DW1 amplitudes are markedly enhanced relative to regular QBO easterly (QBOE) conditions. In the mesosphere and lower thermosphere (MLT), the mean enhancement reaches~1.56 K (~20.5 %) at the equator and ~0.54 K (~14.4 %) at 30° N/S, with peaks of ~2.40 K (~26.5 %) and ~0.87 K (~29.5 %) at the same latitudes. A pronounced increase of the DW1 (1, 1) mode is also evident in the stratosphere (~0.21 K, ~21%). By contrast, the 2020 disruption shows only a modest rise in DW1 amplitude relative to the regular QBOE. In the MLT, the mean enhancement reaches ~0.50 K (~6.0 %) at the equator and ~0.26 K (~7.7 %) at 30°N/S, with peak anomalies of ~0.91 K (~11.6 %) at the equator and ~0.31 K (~14.2 %) at 30° N/S, whereas in the stratosphere the DW1 (1, 1) mode increase ~0.18 K (~17 %).

(3) During the 2016 event, water vapour radiative heating and latent heating increase by ~8 % and ~22 % relative to QBOE. The zonal wind weak latitudinal shear tends to enhance DW1 amplitudes, while gravity waves strengthen DW1 in the subtropics and damp it at the equator. Nevertheless, the stronger shear near ~40 km likely prevents DW1 amplitudes from reaching the levels observed during normal QBO westerly phases.

In contrast, during the 2020 event, only water vapour radiative heating exhibits a clear rise (~5 %), whereas the latent heating is close to the QBOE. The zonal wind latitudinal shear closely resembled those during QBO easterly phases, and the gravity-wave effect was weaker than in 2016. As a result, the combined influence of water-vapor radiative heating and GW drag contribute only to a slight increase in DW1 amplitudes.

This work analyses the feature how the DW1 varies when the highly unusual wind of QBO occurs. This phenomenon which is found in responses at different atmospheric layers suggests an atmosphere coupling process. The observations and model simulations give clear evidence of the connection. The possible link between the lower atmosphere trace gases variation and

MLT dynamic features is shown during these unique events. The result gives a window for exploring the mechanism of the coupling, providing a basis for future research on the underlying mechanisms.

Appendix A: approach for calculating the water vapor radiative heating rate

The heating rate for water vapor mainly follows the method from Groves et al. (1982) and Lieberman et al. (2003). As mentioned in equation 1, the heating rate could be categorized into clear sky and cloudy sky. The equation of clear sky is given by Lacis and Hansen (1974):

$$J_{clr} = q\eta^{c} S_0 \cos\zeta \left[MA(y) + \frac{5}{3}RA(y')\right] \tag{A1}$$

with q is water vapor mixing ratio (specific humidity), η is defined as p/p_0, c is defined as $0.75 - \Gamma R_M/2g$. Γ is the vertical lapse rate, which is 6.5K km^{-1}. R_M is the gas constant for air. g is the acceleration of gravity. S_0 is the solar constant, which is 1353 W m^{-2}. ζ is the solar zenith angle, the equation is:

$$\cos\zeta = \sin\theta \sin\delta + \cos\theta \cos\delta \cos t' \tag{A2}$$

with θ is the latitude, δ is the solar declination. t' is given by following equation:

$$t' = \lambda + \Omega t \tag{A3}$$

with λ is longitude in radiance, Ω is the angular frequency of Earth's rotation. t is the universal time.

M is given by equation:

$$M = \frac{35}{(1224\cos^2\zeta + 1)^{\frac{1}{2}}} \tag{A4}$$

A(y) is given by equation:

$$A(y) = 2.9\left[\frac{0.635 + 0.365Y}{(Y^{0.635} + 5.925y)^2 Y^{0.365}}\right]\mathrm{cm^2 g^{-1}} \tag{A5}$$

with:

$$Y = 1 + 141.5y \tag{A6}$$

and

$$y = M\overline{w} \tag{A7}$$

and

$$y' = M\overline{w}_t + \frac{5}{3}(\overline{w}_t - \overline{w}) \tag{A8}$$

The $\overline{w}$ is the effective water vapor amount, is given by equation:

$$\overline{w} = \int_z^\infty q\rho(p/p_0)^{.75}(T_0/T)^{1/2}dz \qquad (A9)$$

Where ρ is the air density. $\overline{w}_t$ is the total water vapor above the reflecting surface.

The cloudy sky heating rate is given by Groves (1982):

$$J_{cld} = q\eta^c S_0 \cos\zeta Z \qquad (A10)$$

with Z is parameter given by:

$$Z = \sum_i \{ak'[\cosh(\xi_0 + \beta - \xi)) - \cosh(\xi_0 + \beta' - \xi)]/\sinh(\xi_0 + \beta)\}_i \qquad (A11)$$

with ξ is given by:

$$\xi = k'\overline{w} \qquad (A12)$$

$$k' = \frac{5}{3}\alpha(\sigma + k) \qquad (A13)$$

with α, β and β':

$$\alpha = (1-\omega)^{\frac{1}{2}}(1+\omega-2\omega f)^{\frac{1}{2}} \qquad (A14)$$

$$\beta = \frac{1}{2}\ln\{[1+\alpha-\omega f - R\omega(1-f)] \div [1-\alpha-\omega f - R\omega(1-f)]\} \qquad (A15)$$

$$\beta' = \beta + \frac{1}{2}\ln\left[\frac{1-\alpha-\omega f}{1+\alpha-\omega f}\right] \qquad (A16)$$

with single scattering albedo:

$$\omega = \frac{\sigma}{\sigma + k} \qquad (A17)$$

where σ = 40 cm^{-1}, f is 0.925, k and a are given by table 2 from Somerville et al. (1974).

Appendix B: approach for calculating the ozone radiative heating rate

The heating rate for ozone mainly uses the equations from Strobel/Zhu model (Strobel, 1978; Zhu, 1999) and processing method from Xu et a. (2010). The Chappius, Hartley and Huggins bands are as follow:

$$\frac{H_{\mathrm{Ch}}}{[\mathrm{O}_3]} = F_c\sigma_c \exp[-\sigma_c \mathrm{N}_3] \qquad (B1)$$

$$\frac{H_{\mathrm{Ha}}}{[\mathrm{O}_3]} = F_{\mathrm{Ha}}\sigma_{\mathrm{Ha}} \exp[-\sigma_{\mathrm{Ha}} \mathrm{N}_3] \qquad (B2)$$

$$\frac{H_{\mathrm{Hu}}}{[\mathrm{O}_3]} = \frac{1}{M\mathrm{N}_3}\left\{I_1 + (I_2 - I_1)exp\left[-\sigma_{Hu}\mathrm{N}_3 e^{-M\lambda_{long}}\right] - I_2 exp\left[-\sigma_{Hu}\mathrm{N}_3 e^{-M\lambda_{short}}\right]\right\} \qquad (B3)$$

The $[\mathrm{O}_3]$ is the ozone number density while the N_3 is the column density of O_3 along the solar radiation path. For equation B1, the F_c is 370 J m^{-2} s^{-1}, the σ_c is 2.85 $\times 10^{-25}$. For equation B2, the F_{Ha} is 5.13 J m^{-2} s^{-1}, the σ_{Ha} is 8.7 $\times 10^{-22}$ m^{-2}. For equation B3, the I_1 is 0.07 J m^{-2} s^{-1} Å^{-1}, the I_2 is 0.07 J m^{-2} s^{-1} Å^{-1}, M is 0.01273 Å^{-1}, λ_{long} is 2805 Å^{-1}, λ_{short} is 3015 Å^{-1}, σ_{Hu} is 1.15 $\times 10^{-6}$ m^{-2}.

For the heating rate calculation, the ozone density profiles are firstly interpolated to a uniform vertical grid with 1 km spacing from 20 km to 105 km. Then the ozone profiles are processing into zonal mean overlapping latitude bins that are 10 degrees wide with centres offset by 5° from 50°S-50°N. The diurnal variation of the vertical profile of the ozone heating rate in each latitude bin is calculated using the SABER ozone density and equation B1-B3, along with the diurnal variation of solar zenith angle for the specific latitude and day of year.

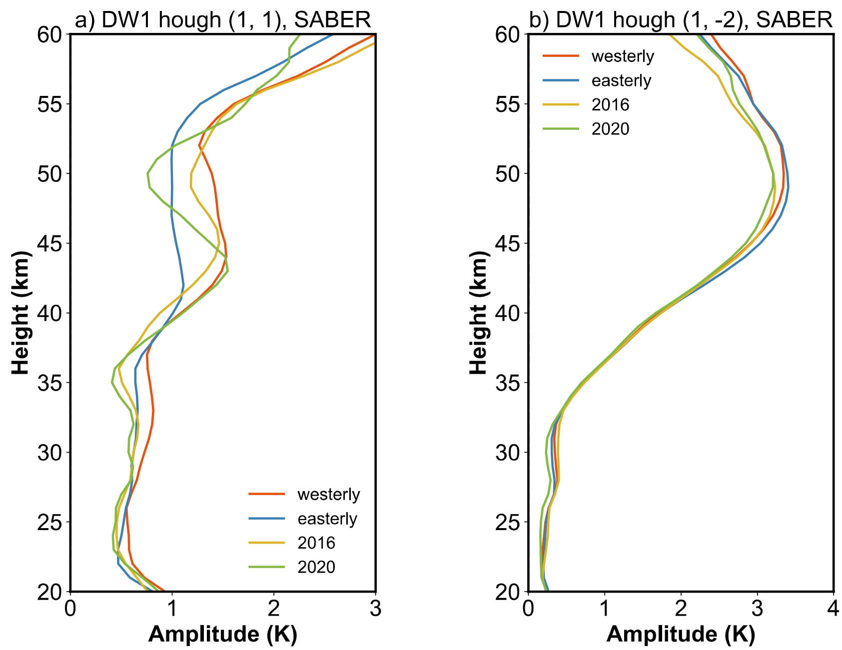

Figure S1. Amplitude profiles of DW1a) (1,1) and b) (1, -2) modes during different QBO phases

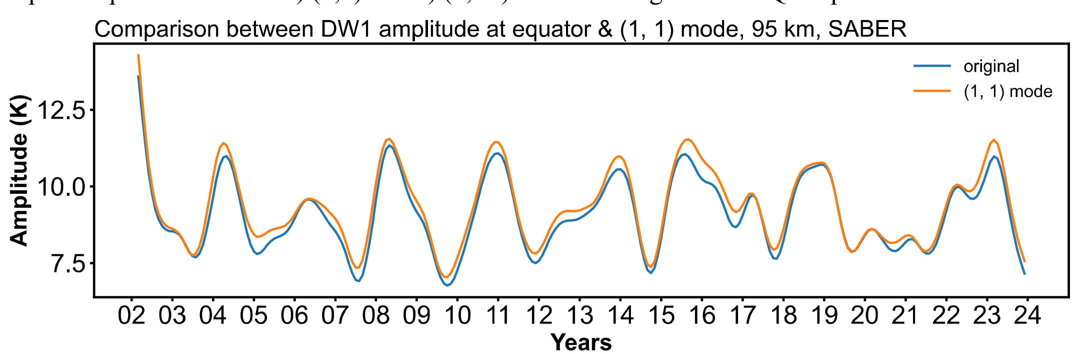

Figure S2. The amplitude time series of equatorial DW1 and (1, 1) Hough mode at 95 km.

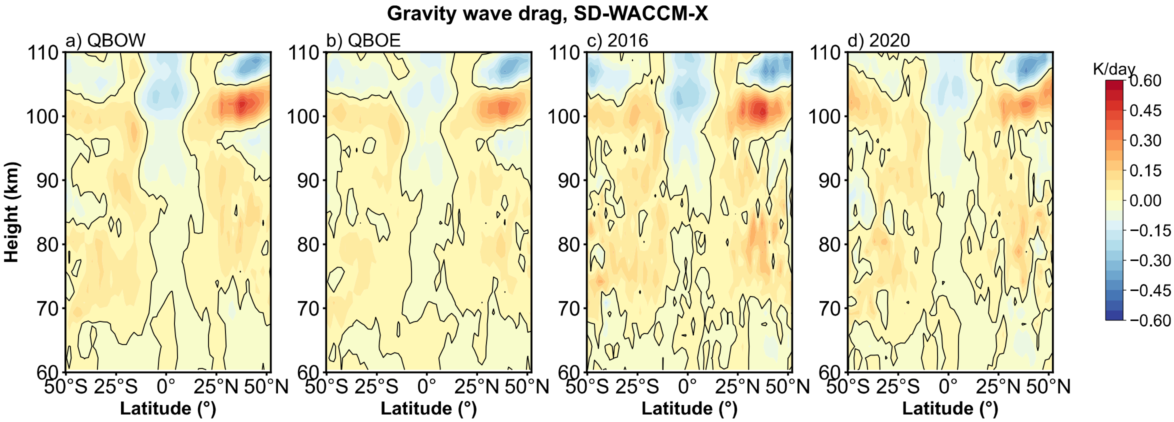

Figure S3. The gravity wave forcing on DW1 during difference QBO phases as a function of latitude and altitude

Data availability. SABER data is available from the SABER project data server at https://spdf.gsfc.nasa.gov/pub/data/timed/saber/. The SD-WACCM-X is retrieved from https://app.globus.org/file-manager?origin_id=d2762023-6ab4-46c9-ab12-b037cd568e42&origin_path=%2F. The QBO index is retrieved from https://acd-ext.gsfc.nasa.gov/Data_services/met/qbo/QBO_Singapore_Uvals_GSFC.txt. The Generalized Lomb-Scargle Periodogram and best-frequency fit method are provided by PyAstronomy (https://github.com/sczesla/PyAstronomy). The MERRA-2 reanalysis data can be retrieved from https://disc.gsfc.nasa.gov/datasets/M2T3NVASM_5.12.4/summary/ (zonal wind, temperature, cloud fraction, specific humidity), https://disc.gsfc.nasa.gov/datasets/M2I3NVAER_5.12.4/summary (air density), https://disc.gsfc.nasa.gov/datasets/M2T1NXRAD_5.12.4/summary (surface albedo), https://disc.gsfc.nasa.gov/datasets/M2T3NPTDT_5.12.4/summary?keywords=MERRA2%20tdt (tendency of air temperature due to moist processes).

Author contributions. Conceptualization: SL, GYJ; investigation: SL; methodology: SL, GYJ; project administration: BXL, GYJ and YJZ; software: SL; supervision: GYJ, BXL and YJZ; validation: BXL, GYJ and YJZ; visualization: SL; writing – original draft preparation: SL; and writing – review and editing: GYJ, BXL, XL, JYX, YJZ and WY. All authors have read and agreed to the published version of the paper.

Competing interests. The authors declare that they have no conflict of interest.

Disclaimer. Publisher's note: Copernicus Publications remains neutral with regard to jurisdictional claims made in the text, published maps, institutional affiliations, or any other geographical representation in this paper. While Copernicus Publications makes every effort to include appropriate place names, the final responsibility lies with the authors.

Acknowledgements. WACCM-X SD output data have been used in this study, and we would like to acknowledge the WACCM-X development group at NCAR/HAO for making the model output publicly available. This work was jointly supported by the Strategic Priority Research Program of the Chinese Academy of Sciences (Grant No. XDB0560000), the Pandeng Program of National Space Science Center CAS, National Key R&D program of China (2023YFB3905100), the Project of Stable Support for Youth Team in Basic Research Field, CAS (YSBR-018), the National Natural Science Foundation of China (42174212), the Chinese Meridian Project, and the Specialized Research Fund for State Key Laboratories.

Financial support. This work was jointly supported by the Strategic Priority Research Program of the Chinese Academy of Sciences (Grant No. XDB0560000), the Pandeng Program of National Space Science Center CAS, National Key R&D program of China (2023YFB3905100), the Project of Stable Support for Youth Team in Basic Research Field, CAS (YSBR-018), the National Natural Science Foundation of China (42174212), the Chinese Meridian Project, and the Specialized Research Fund for State Key Laboratories.

References

Anstey, J. A., Banyard, T. P., Butchart, N., Coy, L., Newman, P. A., Osprey, S., and Wright, C. J.: Prospect of Increased Disruption to the QBO in a Changing Climate, Geophys. Res. Lett., 48, 10.1029/2021gl093058, 2021.

Baldwin, M. P., Gray, L. J., Dunkerton, T. J., Hamilton, K., Haynes, P. H., Randel, W. J., Holton, J. R., Alexander, M. J., Hirota, I., Horinouchi, T., Jones, D. B. A., Kinnersley, J. S., Marquardt, C., Sato, K., and Takahashi, M.: The quasi-biennial oscillation, Rev. Geophys., 39, 179-229, 10.1029/1999rg000073, 2001.

Barton, C. A. and McCormack, J. P.: Origin of the 2016 QBO Disruption and Its Relationship to Extreme El Niño Events, Geophys. Res. Lett., 44, 10.1002/2017gl075576, 2017.

Cen, Y., Yang, C., Li, T., Russell Iii, J. M., and Dou, X.: Suppressed migrating diurnal tides in the mesosphere and lower thermosphere region during El Niño in northern winter and its possible mechanism, Atmos. Chem. Phys., 22, 7861-7874, 10.5194/acp-22-7861-2022, 2022.

Chapman, S. and Lindzen, R.: Atmospheric tides – thermal and gravitational, D. Reidel Publishing Company, Dordrecht, the Netherlands, ISBN 978-94-010-3401-2, 1970.

Coy, L., Newman, P. A., Pawson, S., and Lait, L. R.: Dynamics of the Disrupted 2015/16 Quasi-Biennial Oscillation, J. Clim., 30, 5661-5674, 10.1175/jcli-d-16-0663.1, 2017.

Davis, R. N., Du, J., Smith, A. K., Ward, W. E., and Mitchell, N. J.: The diurnal and semidiurnal tides over Ascension Island (° S, 14° W) and their interaction with the stratospheric quasi-biennial oscillation: studies with meteor radar, eCMAM and WACCM, Atmos. Chem. Phys., 13, 9543-9564, 10.5194/acp-13-9543-2013, 2013.

de Araújo, L. R., Lima, L. M., Jacobi, C., and Batista, P. P.: Quasi-biennial oscillation signatures in the diurnal tidal winds over Cachoeira Paulista, Brazil, J. Atmos. Sol. Terr. Phys., 155, 71-78, 10.1016/j.jastp.2017.02.001, 2017.

Dhadly, M. S., Emmert, J. T., Drob, D. P., McCormack, J. P., and Niciejewski, R. J.: Short-Term and Interannual Variations of Migrating Diurnal and Semidiurnal Tides in the Mesosphere and Lower Thermosphere, J. Geophys. Res.: Space Phys., 123, 7106-7123, 10.1029/2018ja025748, 2018.

Diallo, M., Riese, M., Birner, T., Konopka, P., Müller, R., Hegglin, M. I., Santee, M. L., Baldwin, M., Legras, B., and Ploeger, F.: Response of stratospheric water vapor and ozone to the unusual timing of El Niño and the QBO disruption in 2015–2016, Atmos. Chem. Phys., 18, 13055-13073, 10.5194/acp-18-13055-2018, 2018.

Diallo, M. A., Ploeger, F., Hegglin, M. I., Ern, M., Grooß, J.-U., Khaykin, S., and Riese, M.: Stratospheric water vapour and ozone response to the quasi-biennial oscillation disruptions in 2016 and 2020, Atmos. Chem. Phys., 22, 14303-14321, 10.5194/acp-22-14303-2022, 2022.

Ern, M., Ploeger, F., Preusse, P., Gille, J. C., Gray, L. J., Kalisch, S., Mlynczak, M. G., Russell, J. M., and Riese, M.: Interaction of gravity waves with the QBO: A satellite perspective, J. Geophys. Res.: Atmos., 119, 2329-2355, 10.1002/2013jd020731, 2014.

Forbes, J. M. and Vincent, R. A.: Effects of mean winds and dissipation on the diurnal propagating tide: An analytic approach, Planet. Space Sci., 37, 197-209, 10.1016/0032-0633(89)90007-x, 1989.

Forbes, J. M. and Garrett, H. B.: Seasonal-Latitudinal Structure of the Diurnal Thermospheric Tide, J. Atmos. Sci., 35, 148-159, 10.1175/1520-0469(1978)035<0148:Slsotd>2.0.Co;2, 1978.

Gan, Q., Du, J., Ward, W. E., Beagley, S. R., Fomichev, V. I., and Zhang, S.: Climatology of the diurnal tides from eCMAM30 (1979 to 2010) and its comparison with SABER, Earth Planets Space, 66, 10.1186/1880-5981-66-103, 2014.

Garcia, R. R.: On the Structure and Variability of the Migrating Diurnal Temperature Tide Observed by SABER, J. Atmos. Sci., 80, 687-704, 10.1175/jas-d-22-0167.1, 2023.

Garcia, R. R., Marsh, D. R., Kinnison, D. E., Boville, B. A., and Sassi, F.: Simulation of secular trends in the middle atmosphere, 1950–2003, J. Geophys. Res.: Atmos., 112, 10.1029/2006jd007485, 2007.

Gelaro, R., McCarty, W., Suarez, M. J., Todling, R., Molod, A., Takacs, L., Randles, C., Darmenov, A., Bosilovich, M. G., Reichle, R., Wargan, K., Coy, L., Cullather, R., Draper, C., Akella, S., Buchard, V., Conaty, A., da Silva, A., Gu, W., Kim, G. K., Koster, R., Lucchesi, R., Merkova, D., Nielsen, J. E., Partyka, G., Pawson, S., Putman, W., Rienecker, M., Schubert, S. D., Sienkiewicz, M., and Zhao, B.: The Modern-Era Retrospective Analysis for Research and Applications, Version 2 (MERRA-2), J Clim, Volume 30, 5419-5454, 10.1175/JCLI-D-16-0758.1, 2017.

Groves, G. V.: Hough components of water vapour heating, J. Atmos. Terr. Phys., 44, 281-290, 10.1016/0021-9169(82)90033-2, 1982.

Hagan, M. E.: Comparative effects of migrating solar sources on tidal signatures in the middle and upper atmosphere, J. Geophys. Res.: Atmos., 101, 21213-21222, 10.1029/96jd01374, 1996.

Hagan, M. E., Burrage, M. D., Forbes, J. M., Hackney, J., Randel, W. J., and Zhang, X.: QBO effects on the diurnal tide in the upper atmosphere, Earth Planets Space, 51, 571-578, 10.1186/BF03353216, 1999.

Holton, J. R. and Lindzen, R. S.: An Updated Theory for the Quasi-Biennial Cycle of the Tropical Stratosphere, J. Atmos. Sci., 29, 1076-1080, 10.1175/1520-0469(1972)029<1076:Autftq>2.0.Co;2, 1972.

Hu, S. and Fedorov, A. V.: The extreme El Niño of 2015–2016 and the end of global warming hiatus, Geophys. Res. Lett., 44, 3816-3824, 10.1002/2017gl072908, 2017.

Jiang, G., Xu, J., Shi, J., Yang, G., Wang, X., and Yan, C.: The first observation of the atmospheric tides in the mesosphere and lower thermosphere over Hainan, China, Chin. Sci. Bull., 55, 1059-1066, 10.1007/s11434-010-0084-8, 2010.

Johnston, B. R., Randel, W. J., and Braun, J. J.: Interannual Variability of Tropospheric Moisture and Temperature and Relationships to ENSO Using COSMIC-1 GNSS-RO Retrievals, J. Clim., 35, 7109-7125, 10.1175/jcli-d-21-0884.1, 2022.

Kang, M.-J. and Chun, H.-Y.: Contributions of equatorial waves and small-scale convective gravity waves to the 2019/20 quasi-biennial oscillation (QBO) disruption, Atmos. Chem. Phys., 21, 9839-9857, 10.5194/acp-21-9839-2021, 2021.

Kang, M.-J., Chun, H.-Y., Son, S.-W., Garcia, R. R., An, S.-I., and Park, S.-H.: Role of tropical lower stratosphere winds in quasi-biennial oscillation disruptions, Sci. Adv., 8, 10.1126/sciadv.abm7229, 2022.

Kogure, M. and Liu, H.: DW1 Tidal Enhancements in the Equatorial MLT During 2015 El Niño: The Relative Role of Tidal Heating and Propagation, J. Geophys. Res.: Space Phys., 126, 10.1029/2021ja029342, 2021.

Kogure, M., Liu, H., and Jin, H.: Impact of Tropospheric Ozone Modulation Due To El Niño on Tides in the MLT, Geophys. Res. Lett., 50, 10.1029/2023gl102790, 2023.

Lacis, A. A. and Hansen, J.: A Parameterization for the Absorption of Solar Radiation in the Earth's Atmosphere, J. Atmos. Sci., 31, 118-133, 10.1175/1520-0469(1974)031<0118:Apftao>2.0.Co;2, 1974.

Li, T., She, C. Y., Liu, H. L., Yue, J., Nakamura, T., Krueger, D. A., Wu, Q., Dou, X., and Wang, S.: Observation of local tidal variability and instability, along with dissipation of diurnal tidal harmonics in the mesopause region over Fort Collins, Colorado (41°N, 105°W), J. Geophys. Res.: Atmos., 114, 10.1029/2008jd011089, 2009.

Lieberman, R. S., Ortland, D. A., and Yarosh, E. S.: Climatology and interannual variability of diurnal water vapor heating, J. Geophys. Res.: Atmos., 108, 10.1029/2002jd002308, 2003.

Lieberman, R. S., Riggin, D. M., Ortland, D. A., Nesbitt, S. W., and Vincent, R. A.: Variability of mesospheric diurnal tides and tropospheric diurnal heating during 1997–1998, J. Geophys. Res., 112, 10.1029/2007jd008578, 2007.

Lindzen, R. S. and Holton, J. R.: A Theory of the Quasi-Biennial Oscillation, J. Atmos. Sci., 25, 1095-1107, 10.1175/1520-0469(1968)025<1095:Atotqb>2.0.Co;2, 1968.

Liu, G., Lieberman, R. S., Harvey, V. L., Pedatella, N. M., Oberheide, J., Hibbins, R. E., Espy, P. J., and Janches, D.: Tidal Variations in the Mesosphere and Lower Thermosphere Before, During, and After the 2009 Sudden Stratospheric Warming, J. Geophys. Res.: Space Phys., 126, 10.1029/2020ja028827, 2021.

Liu, H. L. and Hagan, M. E.: Local heating/cooling of the mesosphere due to gravity wave and tidal coupling, Geophys. Res. Lett., 25, 2941-2944, 10.1029/98gl02153, 1998.

Liu, H. L., Bardeen, C. G., Foster, B. T., Lauritzen, P., Liu, J., Lu, G., Marsh, D. R., Maute, A., McInerney, J. M., Pedatella, N. M., Qian, L., Richmond, A. D., Roble, R. G., Solomon, S. C., Vitt, F. M., and Wang, W.: Development and Validation of the Whole Atmosphere Community Climate Model With Thermosphere and Ionosphere Extension (WACCM‐X 2.0), J. Adv. Model. Earth Syst., 10, 381-402, 10.1002/2017ms001232, 2018.

Liu, H. L., Foster, B. T., Hagan, M. E., McInerney, J. M., Maute, A., Qian, L., Richmond, A. D., Roble, R. G., Solomon, S. C., Garcia, R. R., Kinnison, D., Marsh, D. R., Smith, A. K., Richter, J., Sassi, F., and Oberheide, J.: Thermosphere extension of the Whole Atmosphere Community Climate Model, J. Geophys. Res.: Space Phys., 115, 10.1029/2010ja015586, 2010.

Liu, M., Xu, J., Liu, H., and Liu, X.: Possible modulation of migrating diurnal tide by latitudinal gradient of zonal wind observed by SABER/TIMED, Science China Earth Sciences, 59, 408-417, 10.1007/s11430-015-5185-4, 2015.

Liu, S., Jiang, G., Luo, B., Xu, J., Lin, R., Zhu, Y., and Liu, W.: Solar Cycle Dependence of Migrating Diurnal Tide in the Equatorial Mesosphere and Lower Thermosphere, Remote Sens., 16, 10.3390/rs16183437, 2024a.

Liu, Y., Xu, J., Smith, A. K., and Liu, X.: Seasonal and Interannual Variations of Global Tides in the Mesosphere and Lower Thermosphere Neutral Winds: I. Diurnal Tides, J. Geophys. Res.: Space Phys., 129, 10.1029/2023ja031887, 2024b.

Lu, X., Liu, H. L., Liu, A. Z., Yue, J., McInerney, J. M., and Li, Z.: Momentum budget of the migrating diurnal tide in the Whole Atmosphere Community Climate Model at vernal equinox, J. Geophys. Res.: Atmos., 117, n/a-n/a, 10.1029/2011jd017089, 2012.

Lu, X., Liu, A. Z., Swenson, G. R., Li, T., Leblanc, T., and McDermid, I. S.: Gravity wave propagation and dissipation from the stratosphere to the lower thermosphere, J. Geophys. Res.: Atmos., 114, 10.1029/2008jd010112, 2009.

Marsh, D. R., Mills, M. J., Kinnison, D. E., Lamarque, J.-F., Calvo, N., and Polvani, L. M.: Climate Change from 1850 to 2005 Simulated in CESM1(WACCM), J. Clim., 26, 7372-7391, 10.1175/jcli-d-12-00558.1, 2013.

Mayr, H. G., Mengel, J. G., Talaat, E. R., Porter, H. S., and Chan, K. L.: Mesospheric non-migrating tides generated with planetary waves: I. Characteristics, J. Atmos. Sol. Terr. Phys., 67, 959-980, 10.1016/j.jastp.2005.03.002, 2005.

Mayr, H. G., Mengel, J. G., Chan, K. L., and Porter, H. S.: Seasonal variations of the diurnal tide induced by gravity wave filtering, Geophys. Res. Lett., 25, 943-946, 10.1029/98gl00637, 1998.

McLandress, C.: The Seasonal Variation of the Propagating Diurnal Tide in the Mesosphere and Lower Thermosphere. Part I: The Role of Gravity Waves and Planetary Waves, J. Atmos. Sci., 59, 893-906, 10.1175/1520-0469(2002)059<0893:Tsvotp>2.0.Co;2, 2002a.

McLandress, C.: The Seasonal Variation of the Propagating Diurnal Tide in the Mesosphere and Lower Thermosphere. Part II: The Role of Tidal Heating and Zonal Mean Winds, J. Atmos. Sci., 59, 907-922, 10.1175/1520-0469(2002)059<0907:Tsvotp>2.0.Co;2, 2002b.

Mertens, C. J.: SABER observations of mesospheric temperatures and comparisons with falling sphere measurements taken during the 2002 summer MaCWAVE campaign, Geophys. Res. Lett., 31, 10.1029/2003gl018605, 2004.

Mertens, C. J., Mlynczak, M. G., López-Puertas, M., Wintersteiner, P. P., Picard, R. H., Winick, J. R., Gordley, L. L., and Russell, J. M.: Retrieval of mesospheric and lower thermospheric kinetic temperature from measurements of CO215 µm Earth Limb Emission under non-LTE conditions, Geophys. Res. Lett., 28, 1391-1394, 10.1029/2000gl012189, 2001.

Mlynczak, M. G., Hunt, L. A., Garcia, R. R., Harvey, V. L., Marshall, B. T., Yue, J., Mertens, C. J., and Russell, J. M., 3rd: Cooling and Contraction of the Mesosphere and Lower Thermosphere From 2002 to 2021, J Geophys Res Atmos, 127, e2022JD036767, 10.1029/2022JD036767, 2022.

Mlynczak, M. G., Marshall, B. T., Garcia, R. R., Hunt, L., Yue, J., Harvey, V. L., Lopez-Puertas, M., Mertens, C., and Russell, J.: Algorithm Stability and the Long-Term Geospace Data Record From TIMED/SABER, Geophys. Res. Lett., 50, 10.1029/2022gl102398, 2023.

Mukhtarov, P., Pancheva, D., and Andonov, B.: Global structure and seasonal and interannual variability of the migrating diurnal tide seen in the SABER/TIMED temperatures between 20 and 120 km, J. Geophys. Res.: Space Phys., 114, n/a-n/a, 10.1029/2008ja013759, 2009.

Newman, P. A., Coy, L., Pawson, S., and Lait, L. R.: The anomalous change in the QBO in 2015-2016, Geophys. Res. Lett., 43, 8791-8797, 10.1002/2016gl070373, 2016.

Neale, R., Richter, J. H., Conley, A. J., Park, S., Lauritzen, P. H., Gettelman, A., Williamson, D., Rasch, P. J., Vavrus, S. J., Taylor, M. A., Collins, W., Zhang, M., & LIN, S. (2010). Description of the NCAR Community Atmosphere Model (CAM 4.0), 10.5065/GSEB-6470, 2010

Oberheide, J., Forbes, J. M., Häusler, K., Wu, Q., and Bruinsma, S. L.: Tropospheric tides from 80 to 400 km: Propagation, interannual variability, and solar cycle effects, J. Geophys. Res.: Atmos., 114, 10.1029/2009jd012388, 2009.

Ortland, D. A.: Daily estimates of the migrating tide and zonal mean temperature in the mesosphere and lower thermosphere derived from SABER data, J. Geophys. Res.: Atmos., 122, 3754-3785, 10.1002/2016jd025573, 2017.

Osprey, S. M., Butchart, N., Knight, J. R., Scaife, A. A., Hamilton, K., Anstey, J. A., Schenzinger, V., and Zhang, C.: An unexpected disruption of the atmospheric quasi-biennial oscillation, Science, 353, 1424-1427, 10.1126/science.aah4156, 2016.

Pedatella, N.: Ionospheric Variability during the 2020–2021 SSW: COSMIC-2 Observations and WACCM-X Simulations, Atmosphere, 13, 10.3390/atmos13030368, 2022.

Pramitha, M., Kishore Kumar, K., Venkat Ratnam, M., Praveen, M., and Rao, S. V. B.: Disrupted Stratospheric QBO Signatures in the Diurnal Tides Over the Low-Latitude MLT Region, Geophys. Res. Lett., 48, 10.1029/2021gl093022, 2021a.

Pramitha, M., Kumar, K. K., Ratnam, M. V., Praveen, M., and Bhaskara Rao, S. V.: Stratospheric Quasi Biennial Oscillation Modulations of Migrating Diurnal Tide in the Mesosphere and Lower Thermosphere Over the Low and Equatorial Latitudes, J. Geophys. Res.: Space Phys., 126, 10.1029/2020ja028970, 2021b.

Qian, L., Emery, B. A., Foster, B., Lu, G., Maute, A., Richmond, A. D., et al.: The NCAR TIE-GCM: A community model of the coupled thermosphere/ionosphere system. In J. Huba, R. Schunk, & G. Khazanov (Eds.), Modeling the ionosphere-thermosphere system, John Wiley, 73–83, 10.1002/9781118704417.ch7, 2014

Riggin, D. M. and Lieberman, R. S.: Variability of the diurnal tide in the equatorial MLT, J. Atmos. Sol. Terr. Phys., 102, 198-206, 10.1016/j.jastp.2013.05.011, 2013.

Sakazaki, T., Fujiwara, M., and Shiotani, M.: Representation of solar tides in the stratosphere and lower mesosphere in state-of-the-art reanalyses and in satellite observations, Atmos. Chem. Phys., 18, 1437-1456, 10.5194/acp-18-1437-2018, 2018.

Sakazaki, T., Fujiwara, M., and Zhang, X.: Interpretation of the vertical structure and seasonal variation of the diurnal migrating tide from the troposphere to the lower mesosphere, J. Atmos. Sol. Terr. Phys., 105-106, 66-80, 10.1016/j.jastp.2013.07.010, 2013.

Santoso, A., McPhaden, M. J., and Cai, W.: The Defining Characteristics of ENSO Extremes and the Strong 2015/2016 El Niño, Rev. Geophys., 55, 1079-1129, 10.1002/2017rg000560, 2017.

Schoeberl, M. R., Douglass, A. R., Newman, P. A., Lait, L. R., Lary, D., Waters, J., Livesey, N., Froidevaux, L., Lambert, A., Read, W., Filipiak, M. J., and Pumphrey, H. C.: QBO and annual cycle variations in tropical lower stratosphere trace gases from HALOE and Aura MLS observations, J. Geophys. Res.: Atmos., 113, 10.1029/2007jd008678, 2008.

Siddiqui, T. A., Chau, J. L., Stolle, C., and Yamazaki, Y.: Migrating solar diurnal tidal variability during Northern and Southern Hemisphere Sudden Stratospheric Warmings, Earth Planets Space, 74, 10.1186/s40623-022-01661-y, 2022.

Singh, D. and Gurubaran, S.: Variability of diurnal tide in the MLT region over Tirunelveli (8.7°N), India: Consistency between ground- and space-based observations, J. Geophys. Res.: Atmos., 122, 2696-2713, 10.1002/2016jd025910, 2017.

Smith, A. K.: Global Dynamics of the MLT, Surv. Geophys., 33, 1177-1230, 10.1007/s10712-012-9196-9, 2012.

Smith, A. K., Pedatella, N. M., Marsh, D. R., and Matsuo, T.: On the Dynamical Control of the Mesosphere–Lower Thermosphere by the Lower and Middle Atmosphere, J. Atmos. Sci., 74, 933-947, 10.1175/jas-d-16-0226.1, 2017.

Smith, A. K., Harvey, V. L., Mlynczak, M. G., Funke, B., García-Comas, M., Hervig, M., Kaufmann, M., Kyrölä, E., López-Puertas, M., McDade, I., Randall, C. E., Russell, J. M., Sheese, P. E., Shiotani, M., Skinner, W. R., Suzuki, M., and Walker, K. A.: Satellite observations of ozone in the upper mesosphere, J. Geophys. Res.: Atmos., 118, 5803-5821, 10.1002/jgrd.50445, 2013.

Somerville, R. C. J., Stone, P. H., Halem, M., Hansen, J. E., Hogan, J. S., Druyan, L. M., Russell, G., Lacis, A. A., Quirk, W. J., and Tenenbaum, J.: The GISS Model of the Global Atmosphere, J. Atmos. Sci., 31, 84-117, 10.1175/1520-0469(1974)031<0084:Tgmotg>2.0.Co;2, 1974.

Sun, R., Gu, S., Dou, X., and Li, N.: Tidal Structures in the Mesosphere and Lower Thermosphere and Their Solar Cycle Variations, Atmosphere, 13, 10.3390/atmos13122036, 2022.

Stober, G., Kuchar, A., Pokhotelov, D., Liu, H., Liu, H.-L., Schmidt, H., Jacobi, C., Baumgarten, K., Brown, P., Janches, D., Murphy, D., Kozlovsky, A., Lester, M., Belova, E., Kero, J., and Mitchell, N.: Interhemispheric differences of mesosphere–lower thermosphere winds and tides investigated from three whole-atmosphere models and meteor radar observations, Atmos. Chem. Phys., 21, 13855-13902, 10.5194/acp-21-13855-2021, 2021.

Strobel, D. F.: Parameterization of the atmospheric heating rate from 15 to 120 km due to O2 and O3 absorption of solar radiation, J. Geophys. Res.: Oceans, 83, 6225-6230, 10.1029/JC083iC12p06225, 1978.

Tweedy, O. V., Kramarova, N. A., Strahan, S. E., Newman, P. A., Coy, L., Randel, W. J., Park, M., Waugh, D. W., and Frith, S. M.: Response of trace gases to the disrupted 2015–2016 quasi-biennial oscillation, Atmos. Chem. Phys., 17, 6813-6823, 10.5194/acp-17-6813-2017, 2017.

Vincent, R. A., Kovalam, S., Fritts, D. C., and Isler, J. R.: Long-term MF radar observations of solar tides in the low-latitude mesosphere: Interannual variability and comparisons with the GSWM, J. Geophys. Res.: Atmos., 103, 8667-8683, 10.1029/98jd00482, 1998.

Wang, J., Li, N., Yi, W., Xue, X., Reid, I. M., Wu, J., Ye, H., Li, J., Ding, Z., Chen, J., Li, G., Tian, Y., Chang, B., Wu, J., and Zhao, L.: The impact of quasi-biennial oscillation (QBO) disruptions on diurnal tides over the low- and mid-latitude mesosphere and lower thermosphere (MLT) region observed by a meteor radar chain, Atmos. Chem. Phys., 24, 13299-13315, 10.5194/acp-24-13299-2024, 2024.

Wang, Y., Rao, J., Lu, Y., Ju, Z., Yang, J., and Luo, J.: A revisit and comparison of the quasi-biennial oscillation (QBO) disruption events in 2015/16 and 2019/20, Atmos. Res., 294, 10.1016/j.atmosres.2023.106970, 2023.

Wu, D. L., McLandress, C., Read, W. G., Waters, J. W., and Froidevaux, L.: Equatorial diurnal variations observed in UARS Microwave Limb Sounder temperature during 1991–1994 and simulated by the Canadian Middle Atmosphere Model, J. Geophys. Res.: Atmos., 103, 8909-8917, 10.1029/98jd00530, 1998.

Wu, Q., Ortland, D. A., Killeen, T. L., Roble, R. G., Hagan, M. E., Liu, H. L., Solomon, S. C., Xu, J., Skinner, W. R., and Niciejewski, R. J.: Global distribution and interannual variations of mesospheric and lower thermospheric neutral wind diurnal tide: 1. Migrating tide, J. Geophys. Res.: Space Phys., 113, n/a-n/a, 10.1029/2007ja012542, 2008.

Xu, J., Smith, A. K., Jiang, G., and Yuan, W.: Seasonal variation of the Hough modes of the diurnal component of ozone heating evaluated from Aura Microwave Limb Sounder observations, J. Geophys. Res.: Atmos., 115, 10.1029/2009jd013179, 2010.

Xu, J., Smith, A. K., Yuan, W., Liu, H. L., Wu, Q., Mlynczak, M. G., and Russell, J. M.: Global structure and long-term variations of zonal mean temperature observed by TIMED/SABER, J. Geophys. Res., 112, 10.1029/2007jd008546, 2007.

Xu, J., Smith, A. K., Liu, H. L., Yuan, W., Wu, Q., Jiang, G., Mlynczak, M. G., Russell, J. M., and Franke, S. J.: Seasonal and quasi-biennial variations in the migrating diurnal tide observed by Thermosphere, Ionosphere, Mesosphere, Energetics and Dynamics (TIMED), J. Geophys. Res., 114, 10.1029/2008jd011298, 2009.

Yang, C., Smith, A. K., Li, T., and Dou, X.: The Effect of the Madden‐Julian Oscillation on the Mesospheric Migrating Diurnal Tide: A Study Using SD‐WACCM, Geophys. Res. Lett., 45, 5105-5114, 10.1029/2018gl077956, 2018.

Zhu, X.: An Accurate and Efficient Radiation Algorithm for Middle Atmosphere Models, J. Atmos. Sci., 51, 3593-3614, 10.1175/1520-0469(1994)051<3593:Aaaera>2.0.Co;2, 1994.